

Confocal Analysis of CNC based Hydrogels and Suspensions

Aref Abbasi Moud

University of Calgary

Amir Sanati Nezhad (✉ amir.sanatinezhad@ucalgary.ca)

University of Calgary Schulich School of Engineering <https://orcid.org/0000-0002-2309-2388>

Seyed Hossein Hejazi

University of Calgary

Research Article

Keywords: cellulose nano crystals, self-healing, gel collapse, fluorescence recovery after photobleaching (FRAP), confocal laser scanning microscopy (CLSM)

Posted Date: June 2nd, 2021

DOI: <https://doi.org/10.21203/rs.3.rs-529131/v1>

License: © ⓘ This work is licensed under a Creative Commons Attribution 4.0 International License.

[Read Full License](#)

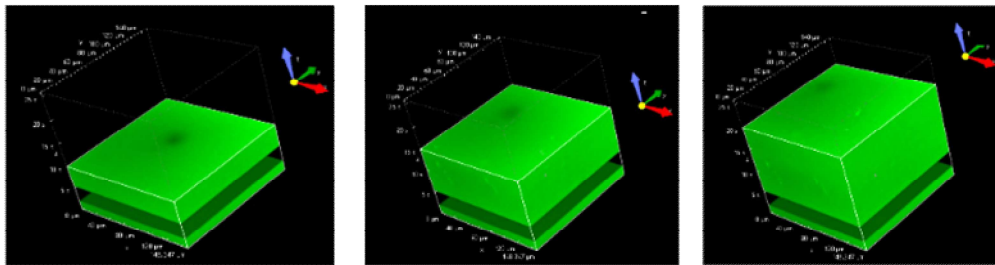
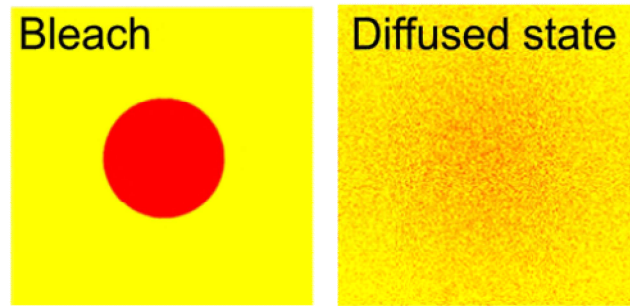
1 Confocal analysis of CNC based hydrogels and suspensions

2 Aref Abbasi Moud,^{a,b†} Amir Sanati-Nezhad,^{b*} Seyed Hossein Hejazi,^{a*}

3 ^a Department of Chemical and Petroleum Engineering, University of Calgary, 2500 University Dr NW,
4 Calgary, Alberta T2N 1N4, Canada

5 ^b BioMEMS and Bioinspired Microfluidic Laboratory, Center for Bioengineering Research and Education,
6 Department of Mechanical and Manufacturing Engineering, University of Calgary, Calgary, Alberta T2N
7 1N4, Canada

8 *Corresponding Authors: E-mail: shhejazi@ucalgary.ca (Seyed Hossein Hejazi),
9 amir.sanatinezhad@ucalgary.ca (Amir Sanati-Nezhad)



10

11

Graphical Abstract:

12 Comparison of simulation and experiment of Fluorescence recovery after photobleaching (FRAP)

13 recovery of CNC suspension

14

15 Abstract

16 Cellulose nano crystal (CNC) hydrogels, while mechanically weak, have unique properties such as easy
17 synthesis, high water content, and biocompatibility. Further improvement is needed to make CNC
18 hydrogels mechanically stable and self-healable. Herein, using quantitative fluorescence recovery after
19 photobleaching (FRAP) analysis, we assess stability, collapse, and level of self-healing of CNC hydrogels
20 with different CNC and sodium chloride (NaCl) concentrations. We use the mean signal intensity obtained
21 by confocal laser scanning microscopy (CLSM) to measure signal loss of the samples made of CNC
22 hydrogels of different CNC concentrations and as a function of initial gel height and NaCl loading. The

23 CNC dynamics inside the gels based on universality curves is unraveled which links the zeta potentials to
24 the immobile particle percentages and the storage moduli as a function of NaCl/CNC concentration ratio.
25 FRAP recovery analysis shows that for the ratio of NaCl/CNC beyond 0.1, the mobility of the ensemble of
26 CNC particles becomes severely restricted. Hydrogel samples with low CNC concentrations (6 g/L and 10
27 g/L) experience a more substantial collapse rate under gravity than the rate observed for samples with a
28 high CNC concentration (30 g/L). Increasing the CNC concentration hinders particle mobility and thus
29 impedes the self-healing process. Quantification of the gel collapse behavior of CNC gel and its self-healing
30 property is critical in many applications, including water and air filters, oil spill sponges, and tissue
31 engineering.

32 **Keywords:** cellulose nano crystals; self-healing; gel collapse; fluorescence recovery after photobleaching
33 (FRAP); confocal laser scanning microscopy (CLSM)

34

35 **1. Introduction**

36 Hydrogels belong to an important class of materials made in a three-dimension (3D) network swollen in
37 the water. These hydrogels have mechanical properties of both fluids and solids (i.e., they display
38 viscoelastic properties). Hydrogels can be formed in a number of ways mainly the construction from tiny
39 particles or polymer molecules through aggregation or cross-linking (Ahmed 2015). Coagulation, a method
40 of micro or nanoparticles self-assembly into 3D structures, starts with a suspension of particles. Colloids, a
41 terminology limited to suspension with the particle range of 1 to 1000 nm, can coagulate into gel fractals
42 in the presence of attractive interactions (Cherhal et al. 2015). The gel network, during and after formation,
43 is under the influence of gravitational stress. Gels after being fully formed, can be still unstable at low filler
44 loading or weak attraction levels, therefore they can dissociate into fragments descending to the bottom of
45 containers (Lamas et al. 2012). Moreover, formation of the gel is also affected by gravity, which may
46 impose a size-limiting strain on the evolving aggregates (Manley et al. 2004) or push sedimentation before
47 a network can form (Allain et al. 1995). The collapse of gel network, made from different materials and
48 under different conditions, can occur due to a wide range of mechanisms (Allain et al. 1995; Blijdenstein
49 et al. 2004; Evans and Starrs 2002; Glasrud et al. 1993; Starrs et al. 2002; Verhaegh et al. 1999; Weeks et
50 al. 2000). The mechanical stability of gels under gravity is important as it can affect gel properties,
51 morphology and function.

52 Qualitatively, collapse can occur at a constant rate or at a rate that decreases with time, interchangeably
53 (Bartlett et al. 2012). Gel collapse undergoes through a slow initial compaction followed by a significant
54 restructuring and rapid sedimentation, which is ultimately transitioned to slow compaction reaching a

55 steady height (Teece et al. 2011). In the case of gels with tunable inter-particle attractions, the collapse
56 dynamics can jump from steady sedimentation to three-stage sedimentation as the inter-particle attraction
57 is decreased (Bartlett et al. 2012). In the literature, the collapse has been attributed to the weak attractions
58 which influences the network aging properties, such as the network response towards gravity over time
59 (Blijdenstein et al. 2004; Evans and Starrs 2002; Kilfoil et al. 2003; Starrs et al. 2002) or to the rheological
60 characteristics of strong attractions (Senis and Allain 1997).

61 For gels formed with short heights and high-volume fractions (i.e., low porous gels), the gel height
62 decreases exponentially in time until reaching a steady height determined by the balance of gravitational
63 stress and network elastic stress. The initial rate of collapse is a decreasing function of volume fraction,
64 which can be modeled using Darcy's law for the collapse of porous materials (Bartlett et al. 2012).
65 Peddireddy et al. (Peddireddy et al. 2016) studied the gelation kinetics and network structure of CNCs in
66 an aqueous solution. They showed that the CNC gel grows through fractal aggregates until it reaches
67 percolation. They observed that the macroscopic sedimentation for CNC concentrations less than 4 g/L and
68 for NaCl concentrations more than 50 mM had a little dependency on the NaCl content due to the
69 gravitational stress.

70 Aside from the effect of gravity on gel formation and stability, the gel self-healing mechanisms have been
71 studied (Deng et al. 2010; Taylor and in het Panhuis 2016). The dynamics of particles in a gel network can
72 be efficiently characterized by the diffusion coefficient, quantified through the fluorescence recovery after
73 photobleaching (FRAP) analysis module of CLSM (Scalettar et al. 1989). In a FRAP experiment,
74 fluorescent species are irreversibly photo-bleached in either a circular or rectangle region of interest (ROI).
75 Thus, one can record the exchange of particles between the bleached and unbleached regimes and then
76 correlate it to the translational diffusion of particles. Bruggen et al. (Van Bruggen et al. 1997)
77 experimentally measured the translational self-diffusion in isotropic dispersion of colloidal rods of bohemite
78 with the length and diameter of 325 nm and 46 nm, respectively. The concentration dependency of the
79 translational diffusion coefficient was evaluated based on the FRAP protocol for volume fractions up to
80 0.22. It was shown that the translational diffusion coefficient is a linear function of volume fraction, up to
81 approximately 0.14, whereas at higher loading levels, the diffusion coefficient decreases to 3% of its initial
82 values at infinite dilution. Seiffert and Oppermann (Seiffert and Oppermann 2005) used FRAP analysis to
83 measure the diffusion coefficient of poly-methyl methacrylate (PMMA) microspheres dyed with
84 rhodamine. Moreover, FRAP was shown to be capable of measuring diffusion coefficients in rapidly
85 diffusing systems (Seiffert and Oppermann 2005). The use of FRAP for measuring diffusion of particles in
86 a solvent with various viscosities has been validated (Braeckmans et al. 2003). Karvinen et al. (Karvinen et
87 al. 2019) studied the FRAP kinetics of fluorescein-labeled dextrans (FITC-dextran) where the mobilities of

88 different hydrogels are distinguished. FRAP analysis is shown to be capable of accurately monitoring the
89 diffusion in various media (Picart et al. 2005; Sustr et al. 2015) and is an practical method to study gel
90 healing due to its versatility and accuracy.

91 In the present study, we observed that the gel network experiences sedimentation at three distinctive CNC
92 concentrations of 6 g/L, 10 g/L and 30 g/L. We use aqueous solutions of charged-stabilized CNCs, where
93 CNC particles are rod-shaped with the measured hydrodynamic diameter of 205 nm. To initiate
94 aggregation, we add a monovalent salt (NaCl) at different concentrations that in some samples it reaches a
95 final concentration of 86.2 mM. At this ionic strength, CNC particles experience a strong Van der Waals
96 attraction, thus primarily undergo diffusion-limited cluster aggregation (DLCA) (Moud et al. 2019). We (i)
97 evaluate the diffusion of CNCs in the suspension and the gel forms and (ii) quantify the CNC-based gel
98 collapse at different CNC and NaCl concentrations. We use CLSM to perform FRAP analysis and measure
99 mobility of CNCs inside the gel quantitatively. To the best of our knowledge, this paper is the first extensive
100 report on probing the diffusion of CNCs inside suspensions of CNCs in dilute, semi-dilute, and concentrated
101 regimes. Finally, we show that there is a connection between the zeta potential, immobile particle
102 percentage, and storage modulus in the CNC hydrogel. This finding paves the way for the optimized
103 engineering of the hydrogel, with the balanced healing ability and mechanical properties. Quantification of
104 the gel collapse behavior of CNC gels and their healing property is critical in applications, such as water
105 and air filters, oil spill sponges, and tissue engineering.

106

107 **2. Experiments**

108 *2.1. Materials*

109 CNCs with the reported length of 100-200 nm and diameter of 5-15 nm is supplied by InnoTech Alberta.
110 Based on the manufacturer datasheet, CNCs are extracted with the acid hydrolysis process and have
111 negative charges. NaCl and FB28 were also purchased from Sigma Aldrich. Role of FB 28, a fluorescent
112 dye that binds efficiently to cellulose (Moud et al. 2018) is employed to track the location of cellulose
113 clusters in the suspensions.

114

115 *2.2. Materials Preparation*

116 We used an ultra-sonication (125 W Qsonica Sonicators Q125 Sonicator, Qsonica) to suspend CNCs in
117 deionized (DI) water for 60 min (the energy input of ~2500 J per gram of suspension). To prevent
118 overheating on the surface of CNCs, the sonication is done in an ice bath (i.e., a bath with constant 0 °C)
119 as the surface charge of CNC particles is sensitive to the temperature (Beck-Candanedo et al. 2005; Pusey
120 1974). The level of dispersion is monitored through tracking the zeta potential values by dynamic light

121 scattering (DLS). It is found that supplying 2,000 joule per gram of CNCs is sufficient for a complete
122 sonication of CNCs which brings down initial CNC clusters to their individualistic sizes. A pH-meter
123 (Mettler-Toledo 135 International Inc., Columbus, OH, USA) is used to adjust pH of the CNC-water
124 suspension to 6.8. The ionic strength of CNC suspension is regulated by the addition of a concentrated 200
125 mM NaCl.

126 We examine the binding of FB28 dye to CNC particles by sonicating them in the DI water and filtering the
127 suspension through a filter paper (Whatman™ Quantitative filter Paper) with the pore size of 100 nm. The
128 approach is adopted from previous works where the binding of FB28 to chitin was demonstrated (Brunner
129 et al. 2009; Ehrlich et al. 2013; Ehrlich et al. 2007). We expect that, in the case of no binding, the FB28 can
130 easily pass through the filter, while CNC particles get trapped. We rinse the filter paper several times with
131 the DI water and inspect the paper under the ultraviolet (UV) light and by a confocal microscopy. **Figure**
132 **S2** shows that after filtration, the separated CNCs captured on the filter maintained FB28 (i.e., FB28 binds
133 to CNC).

134

135 **2.3. Materials Characterization**

136 *2.3.1. Dynamic light scattering*

137 Nano-Zetasizer (Malvern Instruments, Nano ZS, Malvern, UK) is employed to measure the size of CNC
138 particles suspended in the DI water. A He-Ne laser (Spectra Physics 2020, with the wavelength of $\lambda =$
139 633 nm) and a backscatter detection system at 173° is used to capture the dynamics of CNCs. The
140 backscattering detection system that eliminates the multiple scattering phenomena of scattered light allows
141 for measuring the translational diffusion of CNCs of highly concentrated samples (Harding 1999). At a
142 high scattering angle, as opposed to the detection at 90° , the contribution of rotational diffusion is ignored
143 and the translation diffusion is estimated (Harding 1999). For a typical sample of cellulose, the refractive
144 index and the extinction coefficient at 632.8 nm are, respectively, 1.46869 and 0.

145

146 *2.3.2. Confocal laser scanning microscopy*

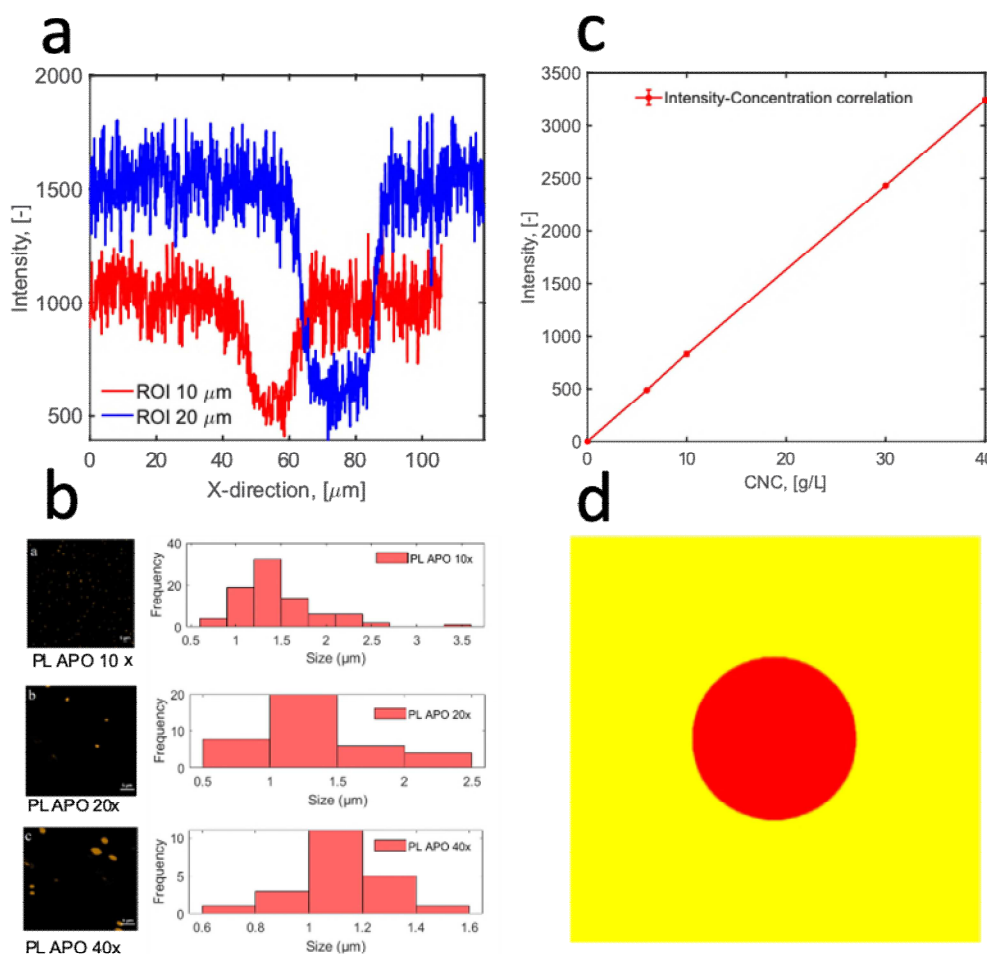
147 We use the FB28 dye for the imaging of CNCs. The dye concentration needs to be selected below a
148 threshold to neither influence the behavior of CNCs nor the gel. In our experiments, for samples with 10
149 g/L CNC concentration, adding up to 500 ppm FB28 does not change zeta potential values of CNCs.
150 However, this dye concentration is sufficient to provide enough fluorescence to CNCs (Zhang et al. 2012).
151 The samples are mixed with dye and then left in the dark atmosphere for approximately 30 min for
152 incubation of the fluorescence dye with CNC particles. CLSM monitoring is performed for suspensions at
153 different NaCl and CNC concentrations. CLSM measurements were carried out with an inverted Nikon

154 confocal microscope (Ti-A1R) equipped with the apochromatic lens objectives of 10X (NA=0.45) and 20X
155 NA=0.75, providing resolutions of 500 and 300 nm, respectively. For 10X optical lens, numerical aperture
156 and working distance were reported 0.45 and 4 while for 20x optical lens, these numbers are 0.75 and 1
157 mm, respectively. The microscope's galvanometer-based scanner enables achieving high-resolution images
158 with up to 4096 x 4096 pixels.

159 In most FRAP experiments, fluorescent species are irreversibly photo-bleached in either a circular or
160 rectangle region of interest (ROI). Thus, one can record the exchange of surrounding unbleached and
161 bleached particles in ROI at a pace controlled by mobility and interaction parameters involved with
162 medium-particle and particle-particle interactions. This phenomenon leads to a recovery of the bleached
163 region. Assuming that all particles are immobile, the recovery would eventually be complete. However, the
164 recovery is not always 100% as some labeled particles in ROI are immobile. These particles neither
165 contribute to the overall recovery nor give up their site for other unbleached particles. Throughout this
166 work, we designated these particles as immobile or immobile particle percentage. CLSM is usually
167 employed to track the temporal evolution of recovery rate using the same laser used for capturing bleaching
168 but operating at different intensity levels. Subsequently, analyzing the information can be done by fitting a
169 model onto fluorescent recovery curves. The underlying assumptions for the FRAP model as well as how
170 it fits vary significantly between different approaches but eventually it boils down to fitting the recovery
171 rate, indicating how species diffuse into the bleached region (Kang et al. 2010).

172 About ten separate FRAPs are normally taken and averaged out to generate a single FRAP recovery curve.
173 To mitigate this issue, 10–30 adjacent points in the slower part of the curve are averaged. This practice
174 generates roughly equally-spaced points along the recovery curve and eliminates the over-weighting of the
175 slower phase of the curve during the fitting process. For all sets of FRAP measurements, we use a laser
176 with the wavelength of 405 nm under 100% laser power for one loop, for a duration of ~1s stimulation.
177 Depending on the recovery rate of samples, different acquisition periods are selected. We select the offset
178 to be zero and adjust the gain to obtain the best resolution. In some cases, the 2x line averaging is also used
179 to reduce the noise. To be able to capture the diffusion of CNC rods, two frame/sec is selected, and the size
180 of the visualization cube is set at $512 \mu\text{m} \times 512 \mu\text{m}$. Pinholes with 1.8 airy units are selected to obtain an
181 optical sectioning value $\sim 16.25 \mu\text{m}$. The determining factor for optical sectioning is the diffraction-limited
182 axial focus dimension. Depending on the numerical aperture and airy pinhole unit, the thickness of optical
183 slices in CLSM can reach the thickness as low as $0.5 \mu\text{m}$. Moreover, the pixel size of $0.29 \mu\text{m}$ and the ROI
184 size of $10 \mu\text{m}$ are chosen. For all measurements, the PL APO 10x (NA=0.45) lens is used. For the FRAP
185 experiments, the concentration ratio of FB28/CNC is fixed at 4×10^{-5} for all CNC samples. The steps of 1
186 μm in z-direction are taken to generate 3-D micrographs of the gel and CNCs in the NaCl-free suspension.

187 In all experiments, samples are placed between two coverslip glasses. Other information such as the
 188 protocol and equations used are discussed in the Supplementary Information section. **Figure 1a** shows the
 189 fluorescent intensity immediately after bleaching of samples with CNC at 45 g/L concentration and 20 mM
 190 NaCl for two selected ROIs with 10 and 20 μm diameter. Considering the width of the bleached ROI with
 191 respect to the rest of the plane and the fact that the suspension or gel is monitored between two glass covers,
 192 the system can be considered uniformly bleached and therefore is 2-dimensional.



193

194 **Figure 1.** Confocal laser scanning microscope (CLSM) for characterization of cellulose nanocrystal (CNC) gels. **(a)**
 195 A linear relationship between the mean CLSM signal and the concentration of cellulose nanocrystals (CNCs). The
 196 concentration ratio CNC/FB28 for all samples is set at 0.01. The measurement is done at 1 mm above the base of petri-
 197 dish. **(b)** Gaussian bleached area (circular) immediately after bleaching in the sample of CNCs with 45 g/L
 198 concentration and 20 mM sodium chloride (NaCl) for two selected regions of interest (ROIs). **(c)** Investigation on
 199 accuracy of confocal microscopy imaging using particles with known sizes. **(d)** The simulation of fluorescence
 200 recovery after photobleaching (FRAP) experiment shown on b using simple two-dimensional (2-D) random walk
 201 diffusion simulation.
 202

203 For gravity collapse experiments, a circular ROI is selected with a nominal diameter of 500 μm . The optical
204 section is 8.2 μm with an optical resolution of 500 nm. The pixel size is 2.32 μm with the pixel dwell time
205 of 2.18 μs . The respective scan size is 512 \times 512 μm and the graphs are captured with PL APO 10x (NA=
206 0.45) under the line averaging of 2X with the pace of 2 fr/s. The laser power is kept constant at 10% total
207 power throughout the whole experiments. Each measurement was repeated 3-6 times under the duration of
208 240 s experiments to generate respective curves. Pinhole is kept constant at 1.8 airy unit in all experiments.

209 2.3.3. *Random walk diffusive simulation of FRAP*

210 To employ colloid as a term for a suspension, the mixture constituent must not settle at all, or it should, at
211 minimum, takes a long time to settle. Moreover, the size of particles suspended inside the continuous phase
212 should vary between approximately 1 nm to 1000 nm. CNCs, due to their diameter being in nanometric
213 size, fulfill the requirement for forming colloids in the water.

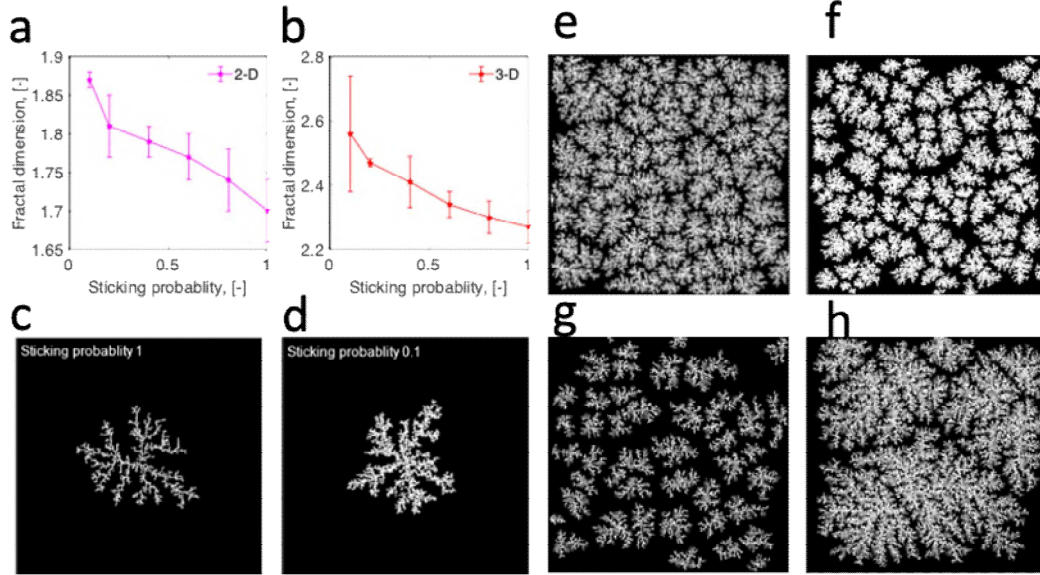
214 The colloidal stability is governed by V , the interaction potential among particles and specifically by the
215 amount of the energy barrier ΔV . If the energy barrier well surpasses the thermal energy, the aggregation
216 would be prevented. On the contrary, if the energy barrier drops below kT (k is the Boltzmann constant and
217 T represents temperature), then aggregation would be initiated, assuming their proximity to other
218 neighboring particles. In the presence of enough salt, the condition of having the energy barrier dipping
219 below kT is dominant, under which CNC particles adhere, and depending on CNC concentration, collapse,
220 or form 3-D gel (Lenfant et al. 2017). For instance, in a study carried out by Cherhal et al. (Cherhal et al.
221 2015), due to the slender shape of CNCs upon the gradual addition of salt, the system changed into a space-
222 filling gel at low concentrations of CNC.

223 A stabilized colloid consists of particles disallowed to aggregate due to repulsive forces. However, when
224 existing repulsive interactive forces become weaker or get screened through the incorporation of a
225 coagulant, particles initiate their aggregation. Accordingly, when the interaction potential acting among
226 particles becomes positive, the aggregation process is limited by solely Brownian diffusion of particles, a
227 regime also known as diffusion-limited aggregation (DLA). Upon reaching to intermediate values, the
228 aggregation becomes slower since a higher number of collisions are needed for their successful aggregation,
229 a regime also known as limited reaction aggregation (RLA). The placement in either of these zones is
230 dependent on the salt concentration in a CNC-salt system.

231 DLA is the process where, due to the Brownian motions, nanoparticles go through the random walk fashion
232 movement and finally cluster together to form aggregates. These clusters are called Brownian trees. Herein,
233 we briefly performed monte Carlo simulations in a lattice for 2-D and 3-D diffusion and found fractal
234 dimensions of clusters. The DLA attachment models of colloids were first introduced by Witten and Sander

235 (Witten Jr and Sander 1981), where a nucleus particle was fixed at a certain point and particles were set
236 loose into the system one after another to migrate onto clusters. Every particle migrates to a neighboring
237 particle in the cluster until it becomes part of it. It is accepted that a cluster formed this way has a self-
238 similarity property in all considered length scales. The fractal dimension associated with these clusters is
239 1.68 ± 0.05 (Meakin 1983) in 2D and 2.5 ± 0.05 (Witten Jr and Sander 1981) in 3D. In DLA simulations,
240 when a particle joins an existing cluster, it becomes stuck. However, if one defines a probability of sticking,
241 the particles would stick to the cluster at a probability between 0 and 1. In the present work, we refer it as
242 sticking probability and found the fractal dimension as a function of sticking probability for 2-D and 3-D
243 simulations (see **Figure 2a-d**). The simulations were conducted with kill zone boundary conditions, and
244 the initial particles number was set at 500000. If the cluster size exceeds the simulation box, the simulation
245 would become terminated. Fractal dimensions were estimated using image J and its box counting module.
246 For each point on the graph, simulations are run 20 times, and the results show average values with the
247 standard deviation. Extending the same concept to higher seed numbers (100 vs 1) leads to the structures
248 simulated in **Figure 2 f-g**. Setting the seeding at 10 leads to the structures shown in **Figure 2 h-i**. The
249 structure is morphologically very dependent on the initial condition of suspension.

250 A similar approach is applied to FRAP experiments, wherein a bleached area is replaced by diffusive
251 surrounding particles. In this simulation, at time zero, the bleach area is set at zero and the unbleached area
252 is set at 1, i.e, a 2-D matrix that comprises 1s and zeros. In the simulation, positions in the matrix occupied
253 by 1 (1s) are given a chance to replace 0s in the matrix. In each simulation step, 1s have the option to move
254 up, down, left and right, in case that they were randomly assigned to move into a position occupied by 1s,
255 then they stay at their position at that simulation step. In cases that 1s or 0s are encountered by the border,
256 they bounce back into the simulation zone. For probing the matrix in one simulation step, positions are
257 swept left to right and in the next step right to left. This sequence ensures that the simulation is governed
258 by a homogenous sweeping.



259

260 **Figure 2.** Fractal dimension and sticking probability. (a-b) Fractal dimension as a function of sticking probability in
 261 2-D and 3-D. (c-d) Depiction of simulated fractal structures with a sticking probability of 1 and 0.1. (e-f) Sticking
 262 probability 0.9 and 0.1 and total seeds 100. (g-h) Setting total seeds at 50 sticking probability 0.9; and setting total
 263 seeds at 10, sticking probability at 0.1 and initial particle numbers at 500000.

264

265

266 3. Results and Discussion

267 3.1 Relationship between CLSM signals strength and CNC concentrations

268 We use a image quantification method to establish a direct relationship between CLSM signal strength and
 269 CNC concentration. The measured CLSM signal (A) is proportional to the fluorescent intensity, and the
 270 absolute values are set by the gain and the laser intensity. The probable values of A may alter within the
 271 range of 0 to 4,050 in integer steps for the images. The gain and the laser intensity are adjusted to have the
 272 picture properly described by the signal distribution while avoiding the pixel saturation. To relate A to CNC
 273 concentration, we determine $f(A)$ for NaCl-free systems labeled with FB28. CNC solutions are
 274 homogeneous on length scale accessible to CLSM so that, on average, the fluorescent intensity remains the
 275 same for all pixels. However, in practice, the dye molecules fluctuate in the plane of focus; hence, the
 276 average fluorescent intensity changes spatially. The width of such fluctuations can be well described by the
 277 normalized standard deviation as equation (1):

$$\sigma = \langle A \rangle^{-1} \sqrt{n^{-1} \sum_{i=1}^n (A_i - \langle A \rangle)^2} \quad (1)$$

278 where $\langle A \rangle$ is spatially averaged signal and A_i is the signal value in pixel i . The smallest value of σ is strictly
279 determined by intensity fluctuations of the dye. It decreases as a function of the illuminated volume if the
280 volume gets bigger or the duration of illumination becomes longer. Typically, the illumination volume is
281 strictly dependent on optics and alters upon a change in lenses. However, it is invariant with respect to the
282 pixel size. The duration of illumination is dependent on scanning speed, i.e., frames taken per unit of time.
283 σ value can be diminished through increasing the FB28 concentration or via averaging the values of
284 repeated experiments. For the case of repeated experiments, care should be taken to keep the dye-CNC
285 concentration spatially identical for the duration of experiments. For the case of solutions with different
286 dye concentrations, the use of similar gain and laser intensity values is not possible. Therefore, it is
287 important to establish a connection between these parameters. Practically, the best route is the determination
288 of absolute signal values using a standard solution, akin to scattering experiments.

289 Here, we use FB28 solutions with known concentrations as the standard. The FB28 concentration needs to
290 be sufficiently high to give a significant signal but not so high where it may alter the structure of CNC gels
291 and their colloidal behavior. The possible influence of FB28 on the structure of CNC gels is investigated by
292 measuring the turbidity of gels containing different amounts of FB28. We find that the structure of CNC
293 gels is not significantly influenced by FB28 for concentrations up to 500 ppm (g/g). Unless specified, we
294 have used the CNC/FB28 concentration equal to 0.01 to obtain the calibration curve for all experiments.
295 The signal and its standard deviation are the same within the experimental error for solutions containing
296 different concentrations of CNC up to 40 g/L and FB28 at a fixed concentration. This implied that binding
297 to CNC does not influence the fluorescent property of FB28. The same observation is made after gel
298 formation. **Figure 1c** shows the average signal intensity as a function of CNC concentration for a
299 concentration ratio of CNC to FB28 equal to 0.01. The mean value of intensity extracted from **Figure 1c**
300 is 489, 833, and 2432 a.u for 6 g/L, 10 g/L, and 30 g/L samples, respectively. A linear relationship is found
301 indicating that A is proportional to C . Practically, establishing a connection between emission intensities
302 and CNC concentrations through a calibration curve is possible using the same solvent (water here),
303 temperature, and pH. The CNC concentration in the system of interest can be determined through
304 comparing emission measurement(s) to the calibration curve and extrapolation. A similar linear
305 relationship is also reported for globular protein b-lactoglobulin concentration (Ako et al. 2009). The CNC
306 concentration-intensity data in Figure 1b indicates that the number of CNCs in each window of confocal
307 observation for a sample of 35 g/L CNC concentration should be 1.75 times higher than a sample of 20 g/L
308 CNC concentration. Due to the gravity collapse or the recovery of photobleached area, we can assign the
309 mean signal value per gram of CNC for finding the changes in concentrations. There are several parameters,
310 such as the depth that the laser travels, the dye concentration, and the quantum yield of the dye that influence

311 the signal detected in the fluorescence spectroscopy. Parameters that have powers to quench the process of
312 fluorescent transition may also influence the fluorescence intensity (Kasha 1952).

313 When discussing the intensity, an important consideration is Beer's Law (i.e., equation 2) (Herman 1998).

$$I = 2.303 K' \varepsilon b C_d P_0 \quad (2)$$

314 where I is fluorescence intensity, ε is molar absorptivity, b is path length, C_d is concentration of the dye
315 molecule, and P_0 is source power. K' is a constant function of several factors, including the cross sectional
316 area of absorption and FB28's quantum yield. The fluorescence intensity changes linearly with the path
317 length the laser travels and with the dye concentration. In equation 2, the fluorescence intensity relates
318 directly to the source power. The higher the source power, the more species that absorb photons and become
319 excited, and depending on the quantum yield of the dye, the more photons that eventually emit in the form
320 of fluorescence radiation. Equation 2 also predicts a linear relationship between the fluorescence intensity
321 and dye concentration. However, the usefulness of this equation levels off at absorbance values of 0.05 or
322 higher, which leads to a negative deviation of the standard curve. Another unique condition of fluorophore
323 containing solutions is that ground-state molecules can reabsorb emitted photons and become excited again.
324 However, upon calibration of the solution containing fluorophore, establishing a connection between the
325 signal intensity and the concentration of dye/CNC is fairly accurate (**Figure 1c**). The ascendant trend of the
326 signal strength at constant laser power, with an increase in CNC concentrations, depicts a perfect
327 distribution of fluorescent agents across the visualization cube (data not shown here).

328 **Figure 1b** attempts to gauge the level of CLSM accuracy based on particles with the known size. We first
329 evaluate the accuracy of CLSM images, where we conduct the calibration experiment using FluoSpheres™
330 Polystyrene Microspheres with a diameter of 1.0 μm and yellow-green fluorescent (505/515). The pictures
331 of particles were taken with PL APO 10x, 20x, and 40x and their corresponding size distribution is shown
332 in **Figure 1b**. The size distributions of $1.46 \pm 0.44 \mu\text{m}$, $1.3 \pm 0.41 \mu\text{m}$ and $1.12 \pm 0.15 \mu\text{m}$ are evaluated for
333 PL APO 10x, 20x and 40x, respectively. The trend shows an improvement in the precision of measurements
334 when lenses with higher magnifications are chosen. Optical resolution given by microscope for PL APO
335 10x, 20x and 40x are 0.69, 0.41 and 0.27 μm , respectively.

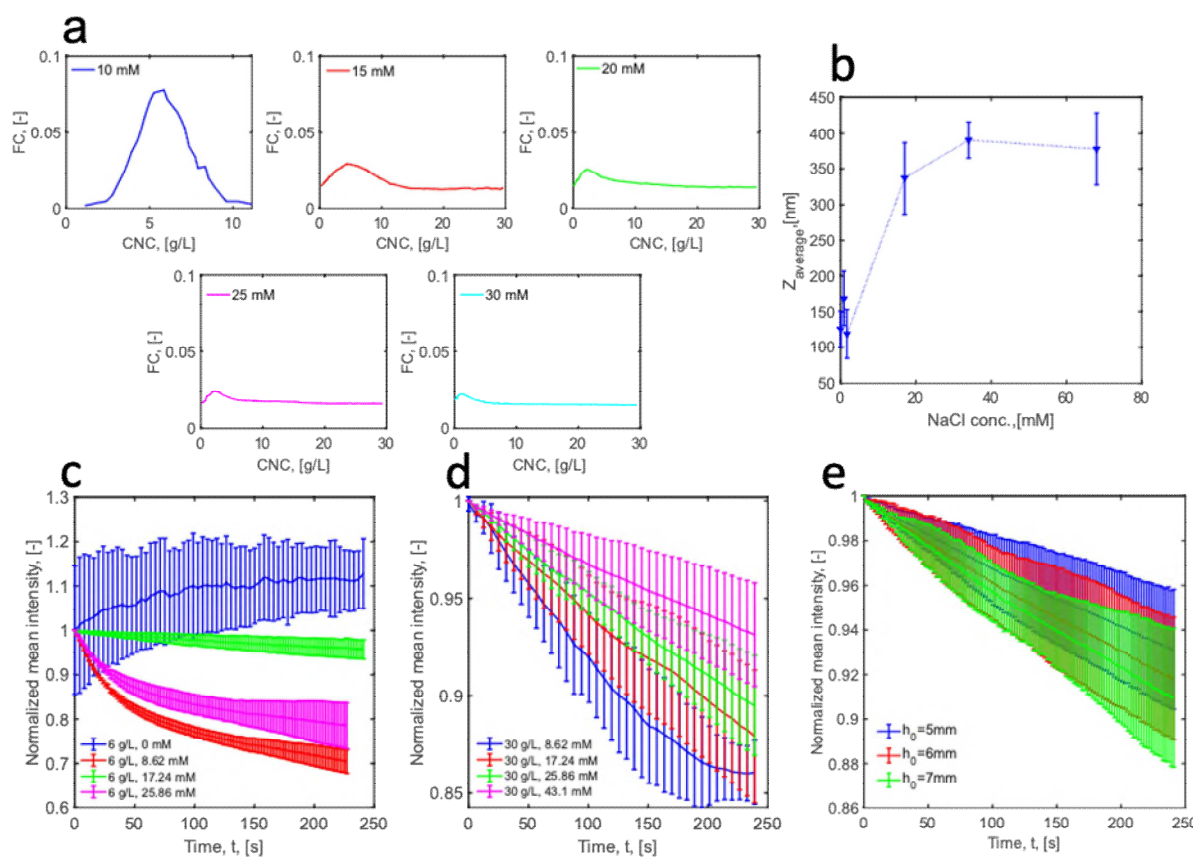
336

337 *3.2 Quantitative analysis of CLSM images of CNC gels*

338 Since A (the measured CLSM signal) is proportional to C , the CNC concentration distribution $f(C)$ is
339 obtained from the signal distribution $f(A)$. **Figure 3a** depicts the variation in CNC-NaCl volume fractions
340 as a function of NaCl concentration and shows the modulation in structural inhomogeneity of CNC
341 following the NaCl addition. These results show that a region with a lower CNC concentration (e.g. original
342 suspension of CNC 5 g/L) tends to occupy more spaces as we increase the NaCl concentrations (10, 15, 20,

343 25, and 30 mM). The clusters grow until they reach a certain size, as $R_c \sim a\varphi^{1/(3-df)}$, at which they span
 344 the space and form a gel (Carpinetti and Giglio 1992). In this equation, R_c is radius of the cluster with df as
 345 fractal dimension and a as size of the primary particles. The results point to the fact that inhomogeneity
 346 occurs across CNC suspensions with increased salt concentration. To shed more light onto cluster sizes of
 347 CNCs at different salt concentrations, dynamic light scattering analysis was carried out. **Figure 3b** shows
 348 that with the addition of only 0-70 mM NaCl into the suspension of CNCs with 0.5 g/L concentration, the
 349 z-average sizes of CNCs grow from 125 nm to 400 nm. These results roughly predict the expected size of
 350 clusters in the gel.

351



352

353 **Figure 3.** Quantitative analysis of CLSM images of CNC gels. (a) CNC concentration distribution for original
 354 suspension of 5 g/L CNC with the addition of NaCl at 10, 15, 20, 25, and 30 mM. (b) depiction of changes in cluster
 355 size of CNCs in the CNC-DI water suspension system on the semi-logarithmic scale following the NaCl addition. The
 356 minimum in the z-factor can be due to the retraction of the double layer. Results were captured at 1 mm above the
 357 base of the petri dish with 10x apo lens (NA=0.45) 5 min after the introduction of NaCl. (c-d) Mean signal intensity
 358 decay for the CNC concentrations of 6 g/L and 30 g/L CNC at 0-43 mM NaCl loadings. The data are captured at 1
 359 mm above the base of the petri dish (the initial gel height is 5 mm) with a 10x apo lens (NA=0.45) and at the timing

360 of 5 min after gelation. (e) Mean signal intensity decay for 30 g/L CNC concentration and 43.1 mM NaCl concentration
361 at different gel initial heights.

362

363 **3.3 Dynamicity of CNC gel toward eventual gel collapse**

364 In our previous study, we demonstrated that gels of the CNC-NaCl hybrid system are very dynamic at the
365 micro-level (Moud et al. 2018). Simulations have also shown that clusters are continuously rearranged and
366 compacted, and form denser structures (Moud et al. 2019). One offshoot of dynamicity is the collapse of
367 CNC gel. In the following, we formulate a framework that can determine, with time, the rate of gel collapse
368 at different height levels. Given the sensitivity of the rate of gel fall to collapse timing, location of the focal
369 plane, and initial gel height, all measurements are done under identical conditions. Moreover, we
370 normalized all graphs with respect to the initial measuring intensity at time zero.

371 The time evolution of normalized mean signal intensity representing the gel collapse with respect to changes
372 in CNC and NaCl concentrations is presented in **Figure 3**. In the case of zero NaCl, the signal intensity
373 fluctuates over 240 s for 6 g/L CNC, which can be due to the Brownian motion of particles that disallow
374 particles to settle. Upon increasing the the NaCl concentration to 17.24 mM and 25.86 mM, the mean
375 intensity decays in time due to the appearance of bigger clusters, which is resulted from negative charges.
376 The size of the cluster at this stage is large enough to shift in the behavior of particles. Moreover, it appears
377 that increased amounts of NaCl enhances the rate of collapse. Unlike the low CNC concentration (6 g/L),
378 the addition of NaCl to a high CNC concentration (30 g/L) decreases the pace of structural decay (**Figure**
379 **3d**). This can be due to gel formation at high CNC concentrations which leads to a higher yield stress in the
380 material. In the report by Danesh et al. (Danesh et al. 2020), the yield stress was probed as a function of
381 salt concentration and the results show that the yield stress increases with addition of more coagulant. In
382 their report for 10 g/L CNC, the addition of 18 mM salt led to the yield stress of 0.21 Pa. This number
383 further increased to 0.34 Pa when the salt content increased to 50 mM. The final normalized mean intensities
384 after 240 s for samples of 8.62, 17.24, 25.86, and 43.1 mM of NaCl are 0.93, 0.89, 0.87 and 0.85,
385 respectively, reflecting that NaCl increases gel resistance towards the gravity effect (higher yield stress).

386 Bartlett et al. (Bartlett et al. 2012) show that gels, fabricated via weak physical bonds, settle under their
387 own weight, following two distinct regimes. For an initial lag time, the formation of a space-spanning
388 network resists compaction. This solid-like behavior persists only for a limited time. However, our
389 experiments show a constant decline in mean signal intensity, suggesting that the macro-scale observations
390 (Bartlett et al. 2012) in microstructural changes cannot be simply extended to the micro-scale.

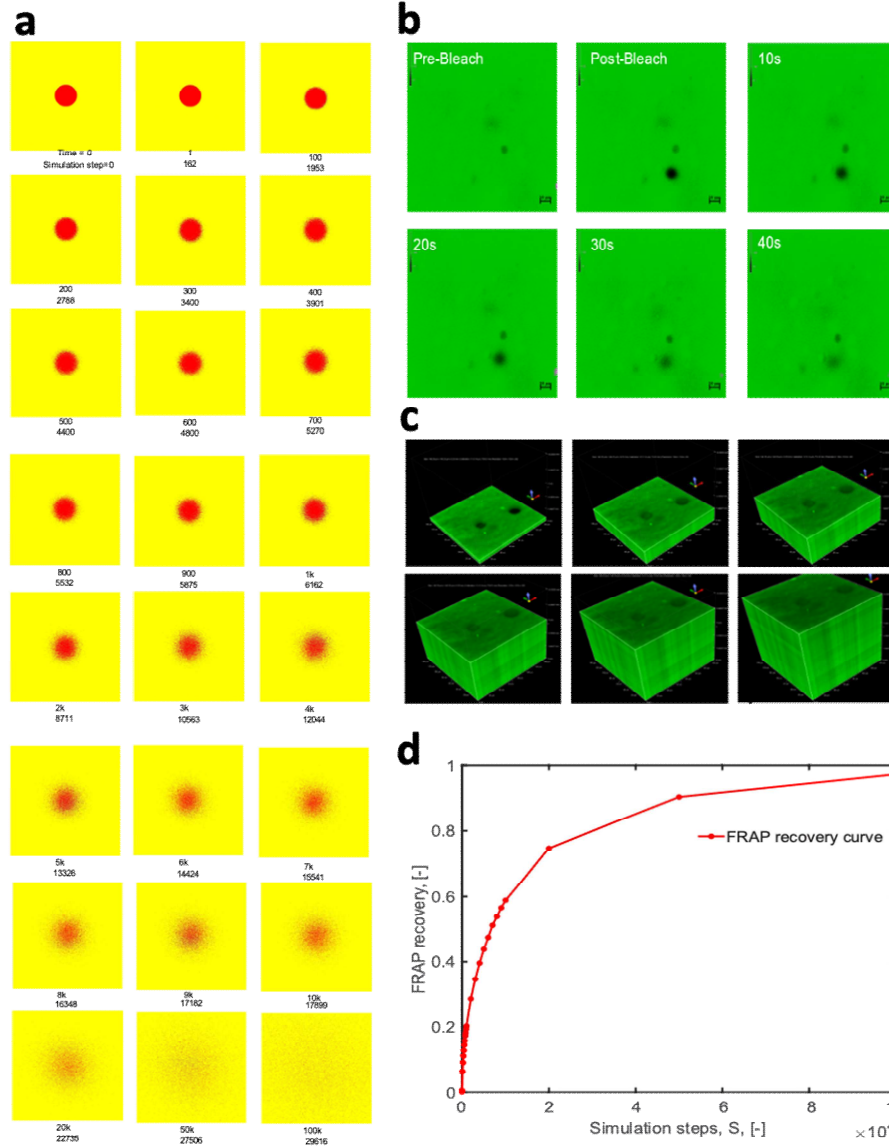
391 For samples of 30 g/L CNC concentration, we previously conducted rheological measurements where after
392 adding 8.5 mM NaCl into the suspension, gelation proceeded, given the condition of $G' > G''$ over the

393 entire frequency range of oscillation (Abbasi Moud et al. 2020) (G' and G'' are storage and loss modulus,
394 respectively, obtained through frequency sweep experiments). Similar reports have also been published
395 recently, corroborating the existence of same trend (Abbasi Moud et al. 2020; Gahrooe et al. 2021; Moud
396 et al. 2019). Therefore, we expect to have gel formation at high CNC concentrations (Here 30 g/L) and in
397 all the NaCl concentrations studied here. The decreasing rate of gel collapse at the increasing NaCl
398 concentration depicts that the gel becomes sturdier (having higher yield stress), which is consistent with the
399 change of the previously reported G' value, where G' was an increasing function of NaCl concentration
400 until it reached a plateau.

401 It is noteworthy to mention that there are slow changes in the average signal intensity with respect to time
402 across the samples. The compaction rate of the gel might be different at macro level versus the micro level.
403 Harich et al. (Harich et al. 2016) reported that the speed of microscopic collapse for poly-
404 methylmethacrylate dispersed in cis-decalin is 8 $\mu\text{m/s}$, which is an order of magnitude higher than the speed
405 of the macroscopic collapse 0.6 $\mu\text{m/s}$. Manely et al. (Manley et al. 2005) showed that the macro scale height
406 of gel exponentially decays in time, where the gel collapse is faster at the higher initial gel height. Our
407 results also confirms the increase of the collapse rate for gels with higher initial height (**Figure 3e**).

408 **Figure 4a** depicts the simulation of FRAP experiments as explained in section 2.3.3 and compares it to the
409 experimental data. After passage of simulation steps of 100k, the state of homogeneity is achieved, i.e
410 density of red and yellow zones is equal across the simulation box. Time series of FRAP images for 45 g/L
411 CNC sample, imaged with PL APO 10x optic (NA=0.45), during 45 s is shown in **Figure 4b**. The sample
412 immobile fraction is 0% after 40 s with ROI size of 10 μm . The FRAP recovery images of 45 g/L CNC
413 sample with 20 mM NaCl over a span of 8.4 min healing process are shown in **Figure 4c**. The results shows
414 that even after passage of 8.4 min, healing is not complete (**Figure 4c**). Asymptotically, after 100k
415 simulation steps, we reached the point that the recovery is close to 1 (**Figure 4d**). The simulation is good
416 method to explore areas that inaccessible through experiments.

417



418

419 **Figure 4.** FRAP simulation and experiment on the recovery of CNC gels. (a) Simulation of FRAP experiment as
 420 explained in section 2.3.3. (b) Experimental investigation of FRAP experiment, Time series of FRAP images for 45
 421 g/L CNC sample imaged with PL APO 10x optic (NA=0.45). The sample immobile fraction is 0% after 40 s. Scale
 422 bar: 10 μm , resolution: 500 nm, ROI size: 10 μm . (c) The FRAP recovery images of the 45 g/L CNC sample with 20
 423 mM NaCl over a span of 8.4 min healing process. The height of the 3-D image shows changes in time that were
 424 continuously captured. The visualization box has the size of 140 μm \times 140 μm . Image resolution: 500 nm. (d) FRAP
 425 recovery generation based on the simulation.

426

427 *3.4 Dynamics of CNC clusters and gels using FRAP*

428 We use FRAP to analyze the extent of CNC particle mobility in the suspension. FRAP measurements can
 429 be easily quantified as a function of the half time recovery ($\tau_{1/2}$), defined as the period required for a bleach

430 spot to recover halfway through between the initial and steady-state fluorescence intensities
 431 (Cheerambathur et al. 2007; Lajoie et al. 2007; Salmon et al. 1984; Stricker et al. 2002). An advantage of
 432 this approach is that $\tau_{1/2}$ can be readily extracted from FRAP recovery curves (Cheerambathur et al. 2007;
 433 Lajoie et al. 2007; Salmon et al. 1984; Stricker et al. 2002). It is noted that the half time recovery can be
 434 affected by experimental parameters such as the nominal radius of the ROI and the bleaching protocol
 435 (Kang et al. 2010); hence, it cannot be used for comparison purposes across studies. Contrary to the half
 436 time recovery, D_{rn} provides a quantitative assess of particle movement through the diffusion (Axelrod et
 437 al. 1976; Soumpasis 1983). Accurate estimates of the diffusion rate are also a vital starting step for the
 438 reaction-diffusion molecular analysis (Kang et al. 2010; Mueller et al. 2010).

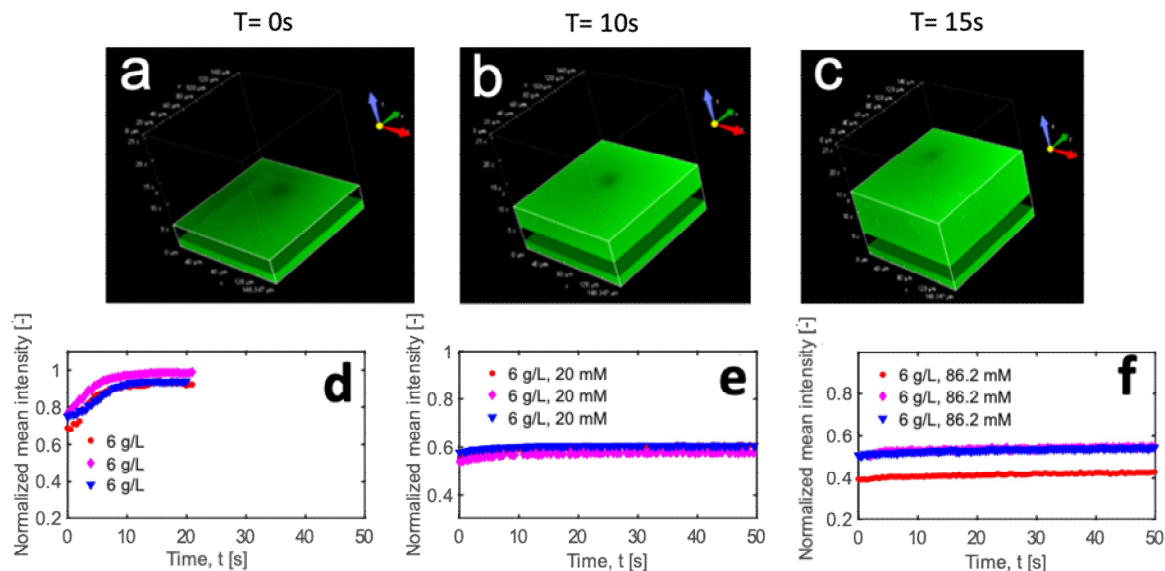
439 We utilize 2D FRAP equations developed by Axelrod for a Gaussian laser (Axelrod et al. 1976) and
 440 Soumpasis (Soumpasis 1983) for uniform circular laser bleaching (Soumpasis 1983). The model relates
 441 D_{rn} , $\tau_{1/2}$ and r_n for an isotropic diffusion system as equation (3):

$$D_{rn} = 0.224 \frac{r_n^2}{\tau_{1/2}} \quad (3)$$

442 where r_n is radius of the bleached area. The constant coefficient 0.224 was numerically determined and
 443 validated. Herein, we follow the protocol provided by Kang et al. (Kang et al. 2010) to adjust equation (3)
 444 for the gaussian bleach profile, as suggested by equation (4). The details of this approach is briefly described
 445 in the Supplementary Information.

$$D_{rn} = \frac{r_n^2 + r_e^2}{8\tau_{1/2}} \quad (4)$$

446
 447 The parameters r_e needs to be determined as the effective radius of the bleached profile. Effective radius
 448 determination occurs through sketching the bleaching profile and obtaining r_e as the radius at 14% of the
 449 bleaching depth. Equation (4) is then used to obtain D_{rn} . **Figures 5(a-c)** show the results of FRAP
 450 experiments for a sample of 6 g/L CNC over a period of 15 s and **Figure 5(d-f)** show the FRAP recovery
 451 curves for a dilute suspension of CNC with 6 g/L concentration at different NaCl concentrations. As
 452 expected, increasing the NaCl concentration retards the mobility of CNCs and increases the population of
 453 immobile particles in the clusters. For example, D_{rn} decreases from 5.5 ± 1.4 to $0.4 \pm 0.28 \mu\text{m}^2/\text{s}$ as NaCl
 454 loading increases from 0 to 86.2 mM. Similar results are observed in other CNC concentrations but with a
 455 different trend.

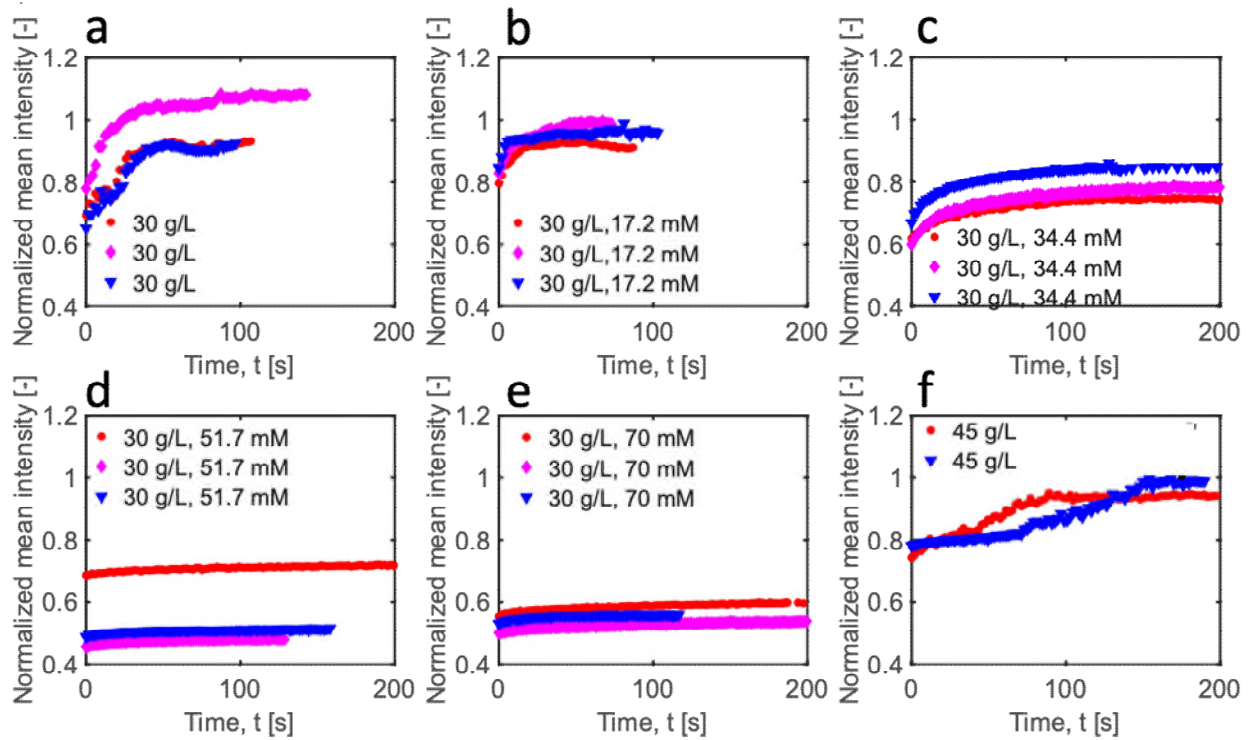


456

457 **Figure 5.** FRAP recovery analysis of low CNC concentration suspensions with the addition of NaCl of different
 458 concentrations. (a-c) FRAP recovery curves for CNC with the concentration of 6 g/L at 0, 20 mM and 86.2 mM NaCl
 459 loadings. (d-e) Temporal-spatial CLSM 3-D images of sample with 6 g/L CNC captured at 0, 10 and 15 s after
 460 bleaching. Visualization box size: 148 $\mu\text{m} \times 148 \mu\text{m}$, resolution: 500 nm.

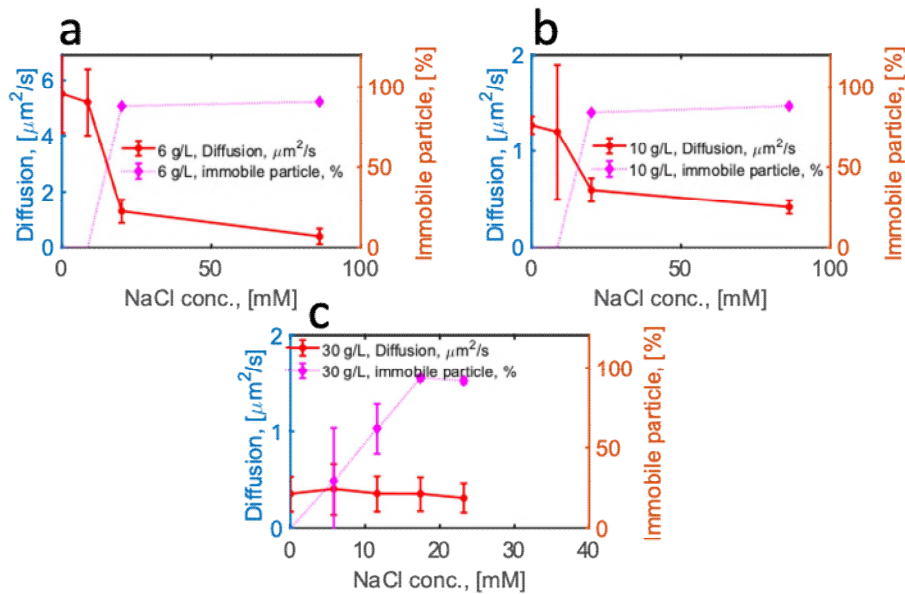
461

462 The FRAP recovery data for higher CNC concentrations of 45 g/L and 30 g/L in the presence of different
 463 concentrations of NaCl is shown in **Figure 6**. D_{rn} is determined to be $0.3 \pm 0.15 \mu\text{m}^2/\text{s}$ based on ten
 464 repetitions at three different points for CNC 30 g/L with 70 mM NaCl. Moreover, the percentage of mobile
 465 particles decreases when the NaCl/CNC concentration ratio passes a certain threshold which is quantified
 466 below. Determining the value of D_{rn} in multiple locations reveals the existence of inhomogeneity in the
 467 gel with regards to the diffusion rate (See Figure 6, graphs in each set of CNC and NaCl concentrations are
 468 sketched in 3 points). This could be attributed to the non-uniform distribution of NaCl during the gelation
 469 process. Jonasson et al. (Jonasson et al. 2008) reported that gels are heterogeneous at the microscale, and
 470 therefore, the local diffusion properties can vary with the position.



471
 472 **Figure 6.** FRAP recovery analysis of high CNC concentration suspensions with addition of NaCl of different
 473 concentrations. **(a-f)** FRAP recovery curves of samples with the CNC concentrations of 45 g/L and 30 g/L at various
 474 concentrations of NaCl (0, 17.2, 34.4, 51.7, 70 mM).

475
 476 The difference in the diffusion coefficients observed at different CNC concentrations (i.e., 6 g/L, 10 g/L,
 477 and 30 g/L) may also be attributed to different degrees of mobility inside the gel network with different
 478 levels of fractal dimensions (**Figure 7**). Immobile particle percentage can be calculated as $(F_i - F_{ss}) / (F_i - F_0)$
 479 where F_i , F_0 and F_{ss} are normalized intensities before bleaching, immediately after bleaching, and at
 480 the steady-state condition, respectively. The fraction of immobile particles is measured to be within the
 481 range of 0-0.91 for different sets of CNC and NaCl loadings (**Figure S3**). For all CNC loadings, there is a
 482 threshold of NaCl concentration, after which the immobile particle percentage increases to about 90% and
 483 D_{rn} decreases. The NaCl concentration lies around 10 mM for 6 g/L CNC concentration and about 20 mM
 484 for 10 g/L and 20 g/L CNC concentrations. Also, the diffusivity of the CNC slows down as the CNC
 485 concentration increases from 6 g/L to 30 g/L (**Figure S3**). This is expected, as the increase in concentration
 486 of the CNC rods hinders CNC particle movements.



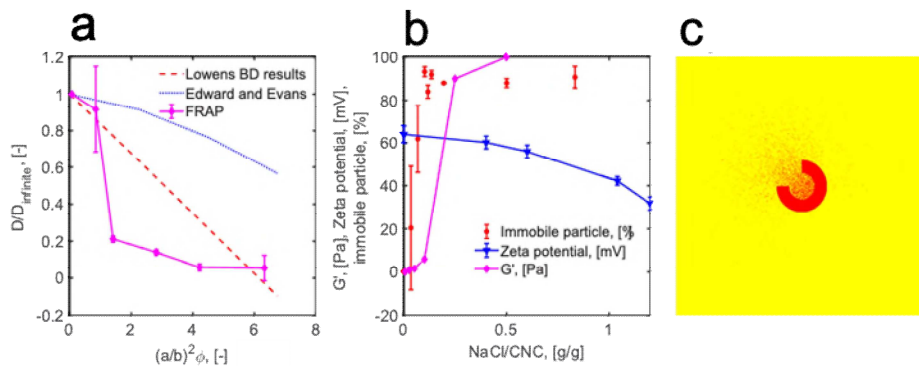
487

488 **Figure 7.** Variation in the diffusion coefficient and immobile particle percentage as a function of NaCl loadings (0,
 489 8.62, 20, 86.2 mM) into the suspensions of (a) 6 g/L CNC, (b) 10 g/L CNC, and (c) 30 g/L CNC concentrations.

490 **Figures S2 and S3** show the healing process after bleaching a sample of 45 g/L CNC concentration without
 491 NaCl and with 20 mM NaCl, respectively. The 3-D FRAP images show changes in the x-y plane while the
 492 height of the 3-D image shows changes in time. The recovery for a CNC suspension without NaCl is fast
 493 (about 20 s) while the addition of NaCl considerably slows down the recovery to even above 8 min.
 494 Studying the role of salt in inhibiting the mobility of particles beside aggregation is out of scope of this
 495 study. The state of CNC aggregation, that can visually aid in envisioning the structure and clusters role in
 496 inhibiting CNC movements, at different level of CNC and NaCl concentration has been reported in our
 497 previous studies (Abbasi Moud et al. 2020; Moud et al. 2019; Moud et al. 2018). Moreover, at 15 g/L CNC
 498 and 10 mM salt, TEM images of clusters in suspension are depicted in **Figure S4**.

499 The diffusion coefficient normalized by the diffusion coefficient at infinite dilution (here at low CNC
 500 concentration of 0.5 g/L) as a function of $(a/b)^2\phi$ in diluted and semi-diluted regimes is shown in **Figure**
 501 **8a**. The results of experimental diffusion testing are also compared to the predictions from the Brownian
 502 dynamics simulations of Lowen and the Edwards and Evans theories (Löwen 1994). The FRAP analysis of
 503 our experimental data along with the theoretical models show that the diffusion is a decreasing function of
 504 particles concentration. The theoretical models overestimate the diffusion values at diluted concentrations.
 505 **Figure 8b** illustrates the universality curves in which the zeta potentials are connected to the immobile
 506 particle percentages and the storage moduli. The region, when there is a dip in absolute values of zeta
 507 potential, is accompanied by a surge in the immobile particle percentage and the storage moduli. This graph
 508 depicts similarities in the trends of studied parameters as a function of NaCl/CNC concentration fraction

509 that manifests CNC dynamics inside the gels. **Figure 8c** depicts systemically how careful selection of
 510 simulation progress leads to partial blockage and delayed diffusion of particles out of their state. Results of
 511 such simulations can be used to further understanding of healing in CNC gel.



512
 513 **Figure 8.** Comparative analysis of FRAP experiments versus other models. **(a)** Measured diffusion coefficients
 514 normalized by $D_{infinite}$, as a function of $(a/b)^2 \phi$. Note that $(a/b)^2 \phi$ is proportional to the number of rods in the
 515 volume L^3 with L the length of the rods. The results of Brownian dynamics and Edwards-Evans equation are also
 516 given as a function of concentration. **(b)** The universality graph that connects data of zeta potential, storage modulus,
 517 and immobile fraction obtained from the FRAP analysis. **(c)** The simulation presenting a path towards realization of
 518 immobile particles blockage effect on the diffusion.

519
 520 The concentration (volume fraction) of particles in the suspension (ϕ) and the aspect ratio (length to
 521 diameter) of rod particles ($r = a/b$) can be used as a criterion to distinguish three regimes of diluted, semi-
 522 diluted, and concentrated networks. Generally, for $\phi \ll (1/r^2)$, rods do not make any contact both
 523 structurally and dynamically, thus the network is dilute. When $1/r^2 \ll \phi \ll (1/r)$, each rod makes a
 524 degree of structural contacts with nearest neighbors, and therefore the network is semi-dilute. Lastly, in the
 525 isotropic concentrated regime $\phi \gg (1/r)$, the rod rotation is both spatially and dynamically hindered by
 526 neighbors where the network is concentrated. Simple models applicable to a single-rod diffusion can be
 527 employed to describe the transition from a freely diffusing regime to a frozen state and ascertain the
 528 influence of rod's geometry. The Doi and Edwards's tube model (Edwards and Evans 1982) can predict the
 529 relationship between the diffusion and concentration of CNCs at diluted and semi-diluted regimes. The tube
 530 model suggests that, with a surge in concentration, rod-shape particles initially lose their ability to move
 531 perpendicular to their long axis. This is reasonable in the semi-diluted regime for rods with a large aspect
 532 ratio. Following that, Edwards and Evans develop a Green's function formalism to calculate the
 533 concentration dependency of particle diffusion parallel to the axis of rods at concentrations around b/a
 534 where b is diameter, and a is length of the particles. Edwards and Evans (Evans and Starrs 2002) considered
 535 the diffusion of a test rod in a hard-rod network. A notable result of their report is that the excluded volume
 536 effects of neighboring rod particles start slowing down significantly the single rod translational diffusion at

537 volume fractions $\varphi \sim (1/r)$. In addition to Edwards and Evans's model (Evans and Starrs 2002), we also
538 use the fitted model to the results of Brownian dynamics simulations for hard spherocylinders, as reported
539 by Lowen (Löwen 1994).

540

541 **Conclusion**

542 This work investigated the dynamics of CNC gel formation, collapse, and self-healing under gravity for
543 various CNC concentrations and salt loadings. To quantify the fluorescence images of three-dimensional
544 CNC hydrogels, we established a relationship between the signal strength and the FB28/CNC
545 concentrations. We evaluated the sample collapse using the mean signal intensity of CLSM where the signal
546 loss, due to the falling of CNC clusters, were quantified for CNCs at concentrations of 6 g/L, 10 g/L, and
547 30 g/L, and at various NaCl loadings. The results show that the signal loss increases in time at low CNC
548 concentration while decreases at a high concentration of 30 g/L CNCs. These opposing trends could be due
549 to the gelation of CNC-NaCl samples at high CNC concentrations. We performed FRAP analysis to probe
550 the diffusion of CNCs at different level of concentrations (i.e., dilute and semi-dilute regimes). After the
551 addition of extra CNCs into a dilute system, the rate of particle diffusion slows down. Furthermore, we
552 measured the rate of CNC particle diffusion in gels and its dependency on CNC and NaCl concentrations.
553 FRAP experiments also show that the system is dynamic at all CNC and NaCl loadings and can be healed
554 regardless of the concentrations. We finally illustrated the connection among immobile particle percentage,
555 zeta potential, and storage modulus through CNC/NaCl concentration ratio. The findings of the present
556 study can pave the path for engineering hydrogels with an optimized level of mechanical properties and
557 healing.

558

559 **Acknowledgements**

560 The authors acknowledge the financial assistance from the Natural Sciences and Engineering Research
561 Council of Canada (NSERC), Alberta Innovates BioSolution's CNC Challenge II and III, and University
562 of Calgary Global Research Initiative in Unconventional Hydrocarbon Resources-Beijing Site.

563

564 **Compliance with ethical approval**

565

566 The authors declare no human participants or animals involved in this research.

567

568

569 **Conflict of interest**

570 The authors declare no competing financial interest.

571

572 **References**

- 573 Abbasi Moud, A., Kamkar, M., Sanati-Nezhad, A., Hejazi, S.H., Sundararaj, U., 2020. Nonlinear
574 viscoelastic characterization of charged cellulose nanocrystal network structure in the presence of salt in
575 aqueous media. *Cellulose* 27, 5729–5743.
- 576 Ahmed, E.M., 2015. Hydrogel: Preparation, characterization, and applications: A review. *Journal of*
577 *Advanced Research* 6(2), 105-121.
- 578 Ako, K., Durand, D., Nicolai, T., Becu, L., 2009. Quantitative analysis of confocal laser scanning
579 microscopy images of heat-set globular protein gels. *Food Hydrocolloids* 23(4), 1111-1119.
- 580 Allain, C., Cloitre, M., Wafra, M., 1995. Aggregation and sedimentation in colloidal suspensions. *Physical*
581 *Review Letters* 74(8), 1478.
- 582 Axelrod, D., Koppel, D., Schlessinger, J., Elson, E., Webb, W.W., 1976. Mobility measurement by analysis
583 of fluorescence photobleaching recovery kinetics. *Biophysical Journal* 16(9), 1055.
- 584 Bartlett, P., Teece, L.J., Faers, M.A., 2012. Sudden collapse of a colloidal gel. *Physical Review E* 85(2),
585 021404.
- 586 Beck-Candanedo, S., Roman, M., Gray, D.G., 2005. Effect of reaction conditions on the properties and
587 behavior of wood cellulose nanocrystal suspensions. *Biomacromolecules* 6(2), 1048-1054.
- 588 Blijdenstein, T.B., van der Linden, E., van Vliet, T., van Aken, G.A., 2004. Scaling behavior of delayed
589 demixing, rheology, and microstructure of emulsions flocculated by depletion and bridging. *Langmuir*
590 20(26), 11321-11328.
- 591 Braeckmans, K., Peeters, L., Sanders, N.N., De Smedt, S.C., Demeester, J., 2003. Three-dimensional
592 fluorescence recovery after photobleaching with the confocal scanning laser microscope. *Biophysical*
593 *Journal* 85(4), 2240-2252.
- 594 Brunner, E., Ehrlich, H., Schupp, P., Hedrich, R., Hunoldt, S., Kammer, M., Machill, S., Paasch, S.,
595 Bazhenov, V., Kurek, D., 2009. Chitin-based scaffolds are an integral part of the skeleton of the marine
596 demosponge *Ianthella basta*. *Journal of Structural Biology* 168(3), 539-547.
- 597 Carpineti, M., Giglio, M., 1992. Spinodal-type dynamics in fractal aggregation of colloidal clusters.
598 *Physical Review Letters* 68(22), 3327.
- 599 Cheerambathur, D.K., Civelekoglu-Scholey, G., Brust-Mascher, I., Sommi, P., Mogilner, A., Scholey, J.M.,
600 2007. Quantitative analysis of an anaphase B switch: predicted role for a microtubule catastrophe gradient.
601 *The Journal of Cell Biology* 177(6), 995-1004.
- 602 Cherhal, F., Cousin, F., Capron, I., 2015. Influence of charge density and ionic strength on the aggregation
603 process of cellulose nanocrystals in aqueous suspension, as revealed by small-angle neutron scattering.
604 *Langmuir* 31(20), 5596-5602.
- 605 Danesh, M., Mauran, D., Hojabr, S., Berry, R., Pawlik, M., Hatzikiriakos, S.G., 2020. Yielding of cellulose
606 nanocrystal suspensions in the presence of electrolytes. *Physics of Fluids* 32(9), 093103.
- 607 Deng, G., Tang, C., Li, F., Jiang, H., Chen, Y., 2010. Covalent cross-linked polymer gels with reversible
608 sol– gel transition and self-healing properties. *Macromolecules* 43(3), 1191-1194.
- 609 Edwards, S., Evans, K., 1982. Dynamics of highly entangled rod-like molecules. *Journal of the Chemical*
610 *Society, Faraday Transactions 2: Molecular and Chemical Physics* 78(1), 113-121.
- 611 Ehrlich, H., Kaluzhnaya, O.V., Brunner, E., Tsurkan, M.V., Ereskovsky, A., Ilan, M., Tabachnick, K.R.,
612 Bazhenov, V.V., Paasch, S., Kammer, M., 2013. Identification and first insights into the structure and
613 biosynthesis of chitin from the freshwater sponge *Spongilla lacustris*. *Journal of Structural Biology* 183(3),
614 474-483.

615 Ehrlich, H., Maldonado, M., Spindler, K.d., Eckert, C., Hanke, T., Born, R., Goebel, C., Simon, P.,
616 Heinemann, S., Worch, H., 2007. First evidence of chitin as a component of the skeletal fibers of marine
617 sponges. Part I. Verongidae (Demospongia: Porifera). *Journal of Experimental Zoology Part B: Molecular
618 and Developmental Evolution* 308(4), 347-356.

619 Evans, R.M.L., Starrs, L., 2002. Emergence of a stress transmission length-scale in transient gels. *Journal
620 of Physics: Condensed Matter* 14(10), 2507.

621 Gahrooe, T.R., Moud, A.A., Danesh, M., Hatzikiriakos, S.G., 2021. Rheological Characterization of CNC-
622 CTAB Network below and above Critical Micelle Concentration (CMC). *Carbohydrate Polymers*, 117552.

623 Glasrud, G., Navarrete, R., Scriven, L., Macosko, C., 1993. Settling behaviors of iron oxide suspensions.
624 *AIChE Journal* 39(4), 560-568.

625 Harding, S., 1999. *Protein Hydrodynamics. Protein: a comprehensive treatise.* JAI Press, Greenwich.

626 Harich, R., Blythe, T., Hermes, M., Zaccarelli, E., Sederman, A., Gladden, L.F., Poon, W.C., 2016.
627 Gravitational collapse of depletion-induced colloidal gels. *Soft Matter* 12(19), 4300-4308.

628 Herman, B., 1998. Fluorescence microscopy. *Current Protocols in Cell Biology*(1), 4.2. 1-4.2. 10.

629 Jonasson, J.K., Lorén, N., Olofsson, P., Nydén, M., Rudemo, M., 2008. A pixel-based likelihood framework
630 for analysis of fluorescence recovery after photobleaching data. *Journal of Microscopy* 232(2), 260-269.

631 Kang, M., Day, C.A., DiBenedetto, E., Kenworthy, A.K., 2010. A quantitative approach to analyze binding
632 diffusion kinetics by confocal FRAP. *Biophysical Journal* 99(9), 2737-2747.

633 Karvinen, J., Ihalainen, T.O., Calejo, M.T., Jönkkäri, I., Kellomäki, M., 2019. Characterization of the
634 microstructure of hydrazone crosslinked polysaccharide-based hydrogels through rheological and diffusion
635 studies. *Materials Science and Engineering: C* 94, 1056-1066.

636 Kasha, M., 1952. Collisional perturbation of spin-orbital coupling and the mechanism of fluorescence
637 quenching. A visual demonstration of the perturbation. *The Journal of Chemical Physics* 20(1), 71-74.

638 Kilfoil, M.L., Pashkovski, E.E., Masters, J.A., Weitz, D., 2003. Dynamics of weakly aggregated colloidal
639 particles. *Philosophical Transactions of the Royal Society of London. Series A: Mathematical, Physical and
640 Engineering Sciences* 361(1805), 753-766.

641 Lajoie, P., Partridge, E.A., Guay, G., Goetz, J.G., Pawling, J., Lagana, A., Joshi, B., Dennis, J.W., Nabi,
642 I.R., 2007. Plasma membrane domain organization regulates EGFR signaling in tumor cells. *The Journal
643 of Cell Biology* 179(2), 341-356.

644 Lamas, B., Abreu, B., Fonseca, A., Martins, N., Oliveira, M., 2012. Assessing colloidal stability of long
645 term MWCNT based nanofluids. *Journal of Colloid and Interface Science* 381(1), 17-23.

646 Lenfant, G., Heuzey, M.-C., van de Ven, T.G.M., Carreau, P.J., 2017. A comparative study of ECNC and
647 CNC suspensions: effect of salt on rheological properties. *Rheologica Acta* 56(1), 51-62.

648 Löwen, H., 1994. Brownian dynamics of hard spherocylinders. *Physical Review E* 50(2), 1232.

649 Manley, S., Cipelletti, L., Trappe, V., Bailey, A., Christianson, R.J., Gasser, U., Prasad, V., Segre, P.,
650 Doherty, M., Sankaran, S., 2004. Limits to gelation in colloidal aggregation. *Physical Review Letters*
651 93(10), 108302.

652 Manley, S., Skotheim, J., Mahadevan, L., Weitz, D.A., 2005. Gravitational collapse of colloidal gels.
653 *Physical Review Letters* 94(21), 218302.

654 Meakin, P., 1983. Diffusion-controlled deposition on fibers and surfaces. *Physical Review A* 27(5), 2616.

655 Moud, A.A., Arjmand, M., Liu, J., Yang, Y., Sanati-Nezhad, A., Hejazi, S.H., 2019. Cellulose nanocrystal
656 structure in the presence of salts. *Cellulose* 26(18), 9387-9401.

657 Moud, A.A., Arjmand, M., Yan, N., Nezhad, A.S., Hejazi, S.H., 2018. Colloidal behavior of cellulose
658 nanocrystals in presence of sodium chloride. *ChemistrySelect* 3(17), 4969-4978.

659 Mueller, F., Mazza, D., Stasevich, T.J., McNally, J.G., 2010. FRAP and kinetic modeling in the analysis of
660 nuclear protein dynamics: what do we really know? *Current Opinion in Cell Biology* 22(3), 403-411.

661 Peddireddy, K.R., Capron, I., Nicolai, T., Benyahia, L., 2016. Gelation kinetics and network structure of
662 cellulose nanocrystals in aqueous solution. *Biomacromolecules* 17(10), 3298-3304.

663 Picart, C., Mutterer, J., Arntz, Y., Voegel, J.C., Schaaf, P., Senger, B., 2005. Application of fluorescence
664 recovery after photobleaching to diffusion of a polyelectrolyte in a multilayer film. *Microscopy Research
665 and Technique* 66(1), 43-57.

666 Pusey, P., 1974. Photon correlation and light beating spectroscopy. Plenum Press, New York.
667 Salmon, E., Leslie, R., Saxton, W., Karow, M., McIntosh, J., 1984. Spindle microtubule dynamics in sea
668 urchin embryos: analysis using a fluorescein-labeled tubulin and measurements of fluorescence
669 redistribution after laser photobleaching. *The Journal of Cell Biology* 99(6), 2165-2174.
670 Scalettar, B.A., Hearst, J.E., Klein, M.P., 1989. FRAP and FCS studies of self-diffusion and mutual
671 diffusion in entangled DNA solutions. *Macromolecules* 22(12), 4550-4559.
672 Seiffert, S., Oppermann, W., 2005. Systematic evaluation of FRAP experiments performed in a confocal
673 laser scanning microscope. *Journal of Microscopy* 220(1), 20-30.
674 Senis, D., Allain, C., 1997. Scaling analysis of sediment equilibrium in aggregated colloidal suspensions.
675 *Physical Review E* 55(6), 7797.
676 Soumpasis, D., 1983. Theoretical analysis of fluorescence photobleaching recovery experiments.
677 *Biophysical Journal* 41(1), 95-97.
678 Starrs, L., Poon, W., Hibberd, D., Robins, M., 2002. Collapse of transient gels in colloid-polymer mixtures.
679 *Journal of Physics: Condensed Matter* 14(10), 2485.
680 Stricker, J., Maddox, P., Salmon, E., Erickson, H.P., 2002. Rapid assembly dynamics of the Escherichia
681 coli FtsZ-ring demonstrated by fluorescence recovery after photobleaching. *Proceedings of the National*
682 *Academy of Sciences* 99(5), 3171-3175.
683 Sustr, D., Duschl, C., Volodkin, D., 2015. A FRAP-based evaluation of protein diffusion in polyelectrolyte
684 multilayers. *European Polymer Journal* 68, 665-670.
685 Taylor, D.L., in het Panhuis, M., 2016. Self-healing hydrogels. *Advanced Materials* 28(41), 9060-9093.
686 Teece, L.J., Faers, M.A., Bartlett, P., 2011. Ageing and collapse in gels with long-range attractions. *Soft*
687 *Matter* 7(4), 1341-1351.
688 Van Bruggen, M., Lekkerkerker, H., Dhont, J., 1997. Long-time translational self-diffusion in isotropic
689 dispersions of colloidal rods. *Physical Review E* 56(4), 4394.
690 Verhaegh, N.A., Asnaghi, D., Lekkerkerker, H.N., 1999. Transient gels in colloid-polymer mixtures
691 studied with fluorescence confocal scanning laser microscopy. *Physica A: Statistical Mechanics and its*
692 *Applications* 264(1-2), 64-74.
693 Weeks, J.R., van Duijneveldt, J.S., Vincent, B., 2000. Formation and collapse of gels of sterically stabilized
694 colloidal particles. *Journal of Physics: Condensed Matter* 12(46), 9599.
695 Witten Jr, T., Sander, L.M., 1981. Diffusion-limited aggregation, a kinetic critical phenomenon. *Physical*
696 *Review Letters* 47(19), 1400.
697 Zhang, Y.P., Chodavarapu, V.P., Kirk, A.G., Andrews, M.P., 2012. Nanocrystalline cellulose for covert
698 optical encryption. *Journal of Nanophotonics* 6(1), 063516.

699

Figures

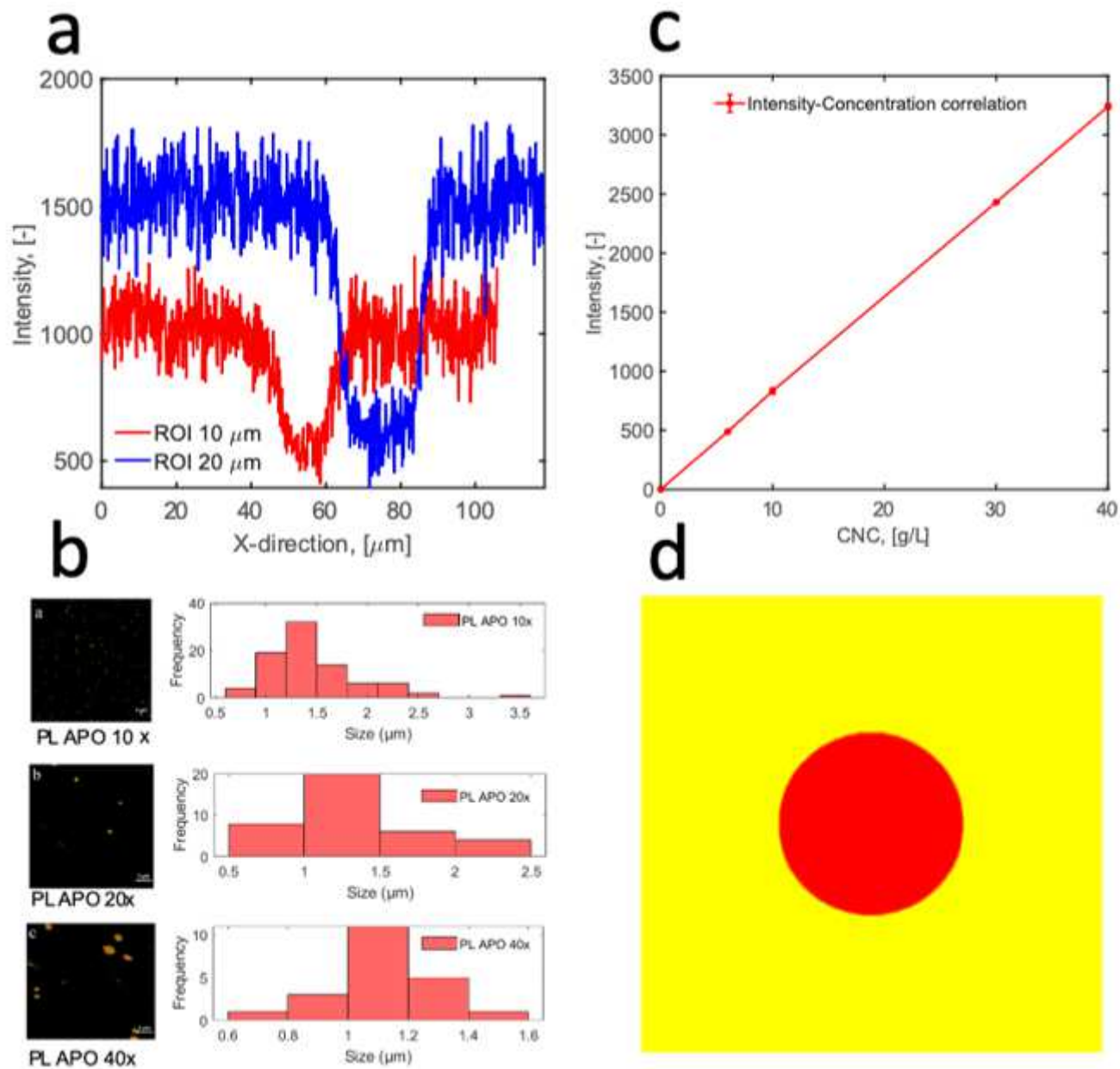


Figure 1

Confocal laser scanning microscope (CLSM) for characterization of cellulose nanocrystal (CNC) gels. (a) A linear relationship between the mean CLSM signal and the concentration of cellulose nanocrystals (CNCs). The concentration ratio CNC/FB28 for all samples is set at 0.01. The measurement is done at 1 mm above the base of petri-dish. (b) Gaussian bleached area (circular) immediately after bleaching in the sample of CNCs with 45 g/L concentration and 20 mM sodium chloride (NaCl) for two selected regions of interest (ROIs). (c) Investigation on accuracy of confocal microscopy imaging using particles with known sizes. (d) The simulation of fluorescence recovery after photobleaching (FRAP) experiment shown on b using simple two-dimensional (2-D) random walk diffusion simulation.

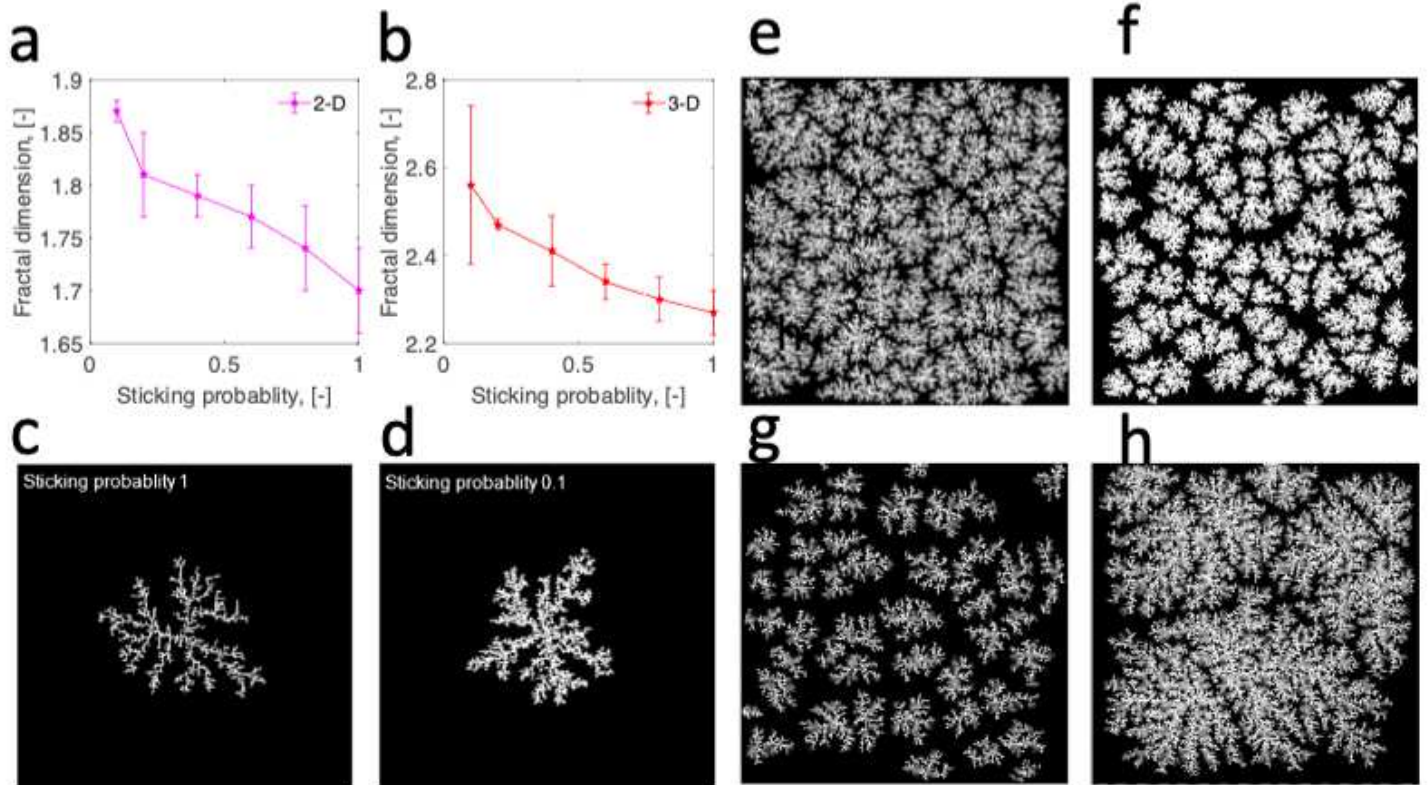


Figure 2

Fractal dimension and sticking probability. (a-b) Fractal dimension as a function of sticking probability in 2-D and 3-D. (c-d) Depiction of simulated fractal structures with a sticking probability of 1 and 0.1. (e-f) Sticking probability 0.9 and 0.1 and total seeds 100. (g-h) Setting total seeds at 50 sticking probability 0.9; and setting total seeds at 10, sticking probability at 0.1 and initial particle numbers at 500000.

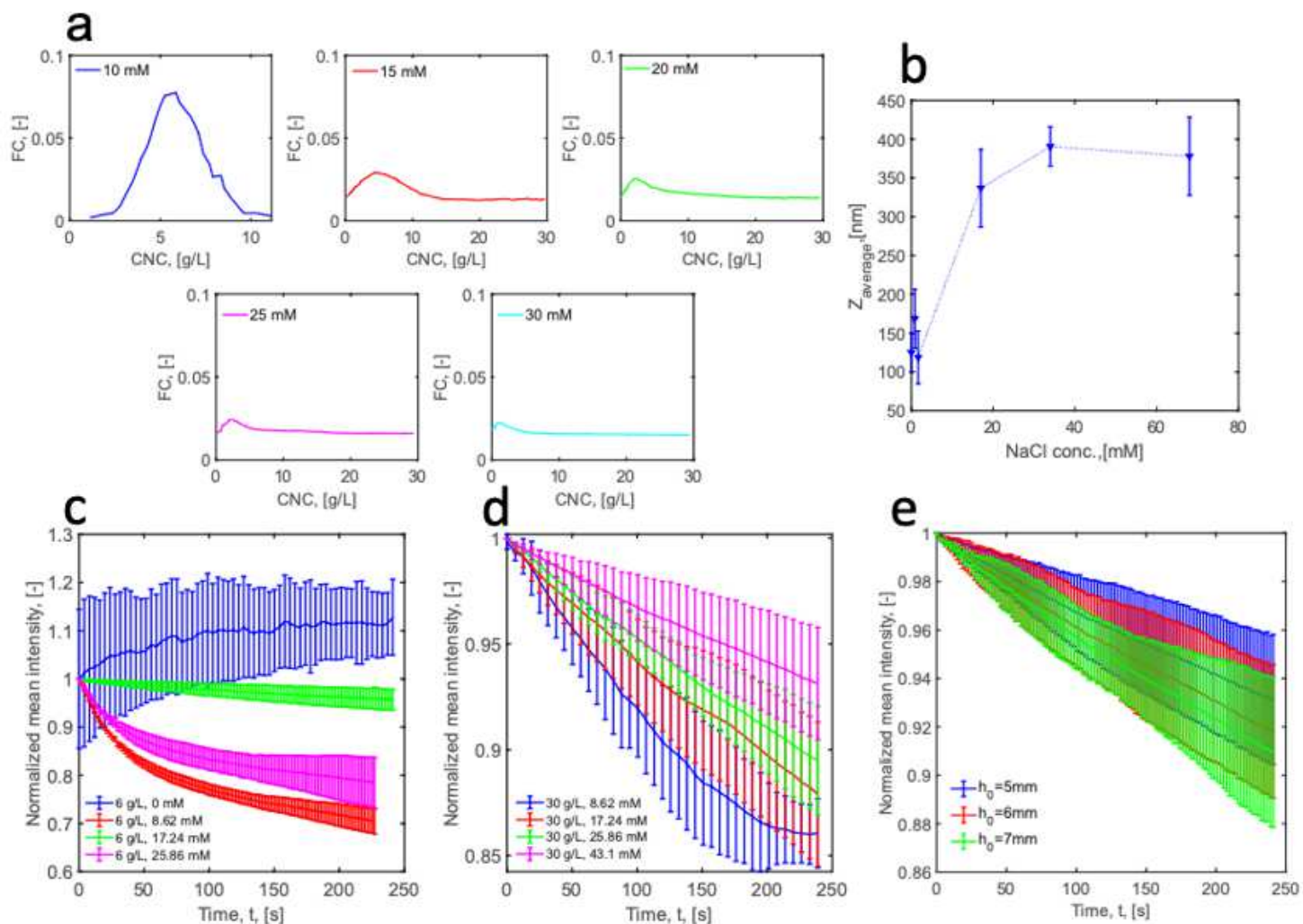


Figure 3

Quantitative analysis of CLSM images of CNC gels. (a) CNC concentration distribution for original suspension of 5g/L CNC with the addition of NaCl at 10, 15, 20, 25, and 30 mM. (b) depiction of changes in cluster size of CNCs in the CNC-DI water suspension system on the semi-logarithmic scale following the NaCl addition. The minimum in the z-factor can be due to the retraction of the double layer. Results were captured at 1 mm above the base of the petri dish with 10x apo lens (NA=0.45) 5 min after the introduction of NaCl. (c-d) Mean signal intensity decay for the CNC concentrations of 6 g/L and 30 g/L CNC at 0-43 mM NaCl loadings. The data are captured at 1 mm above the base of the petri dish (the initial gel height is 5 mm) with a 10x apo lens (NA=0.45) and at the timing of 5 min after gelation. (e) Mean signal intensity decay for 30 g/L CNC concentration and 43.1 mM NaCl concentration at different gel initial heights.

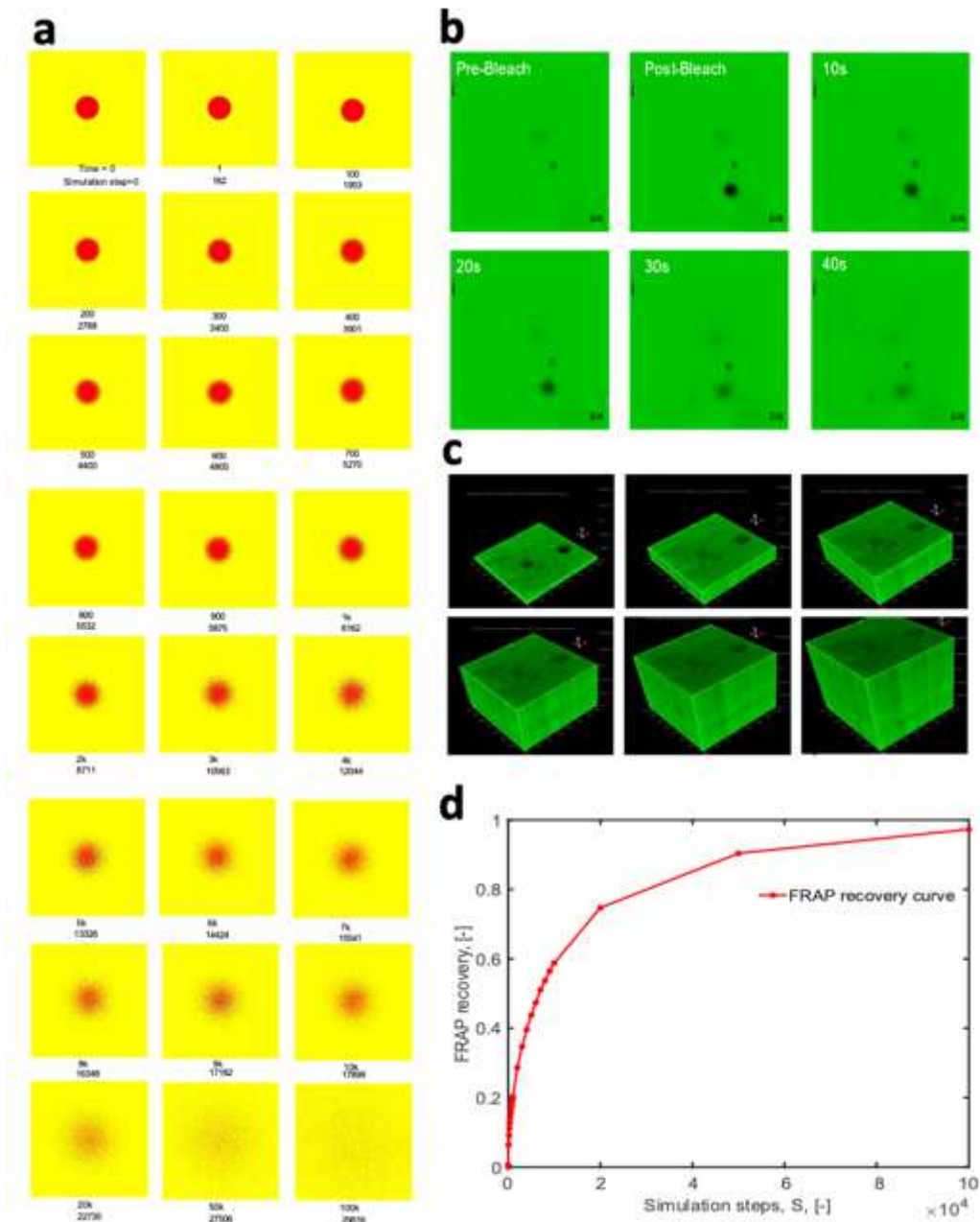


Figure 4

FRAP simulation and experiment on the recovery of CNC gels. (a) Simulation of FRAP experiment as explained in section 2.3.3. (b) Experimental investigation of FRAP experiment, Time series of FRAP images for 45 g/L CNC sample imaged with PL APO 10x optic (NA=0.45). The sample immobile fraction is 0% after 40 s. Scale bar: 10 μm , resolution: 500 nm, ROI size: 10 μm . (c) The FRAP recovery images of the 45 g/L CNC sample with 20 mM NaCl over a span of 8.4 min healing process. The height of the 3-D image shows changes in time that were continuously captured. The visualization box has the size of 140 $\mu\text{m} \times 140 \mu\text{m}$. Image resolution: 500 nm. (d) FRAP recovery generation based on the simulation.

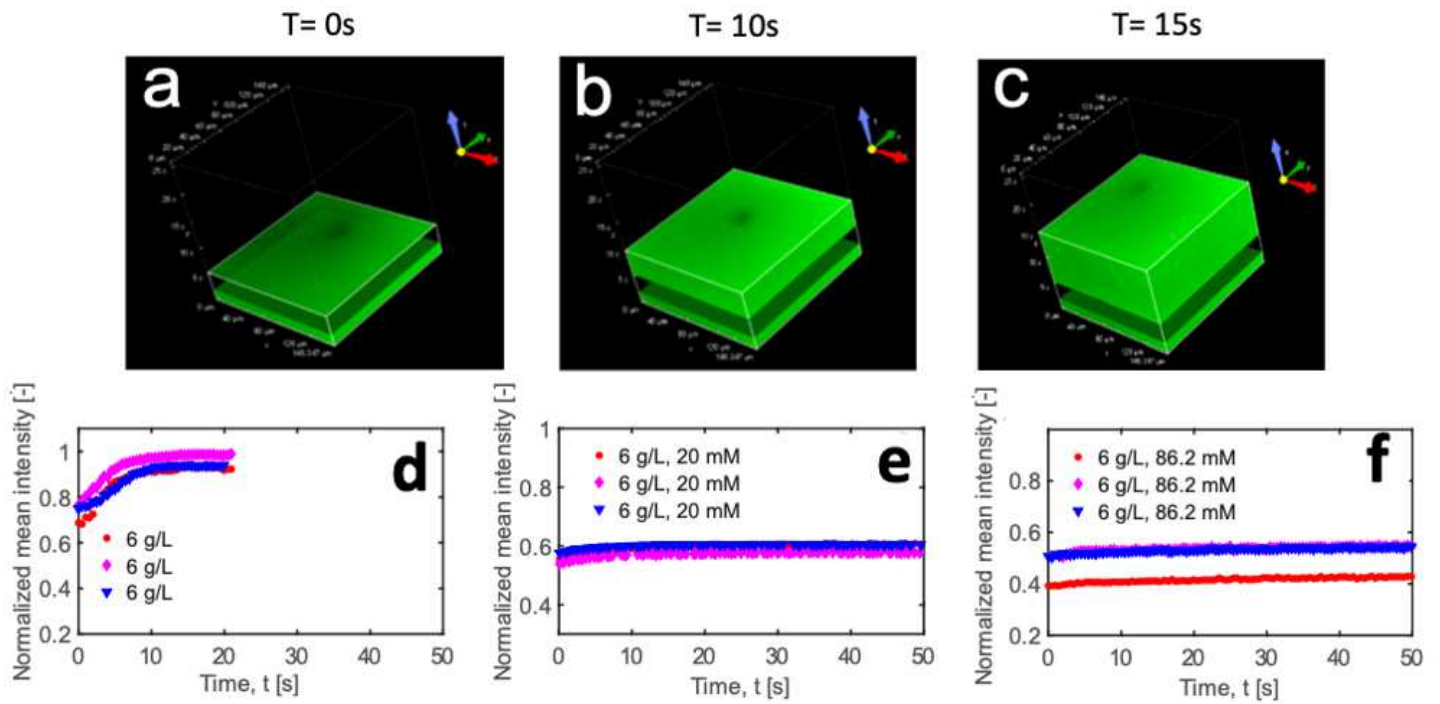


Figure 5

FRAP recovery analysis of low CNC concentration suspensions with the addition of NaCl of different concentrations. (a-c) FRAP recovery curves for CNC with the concentration of 6 g/L at 0, 20 mM and 86.2 mM NaCl loadings. (d-e) Temporal-spatial CLSM 3-D images of sample with 6 g/L CNC captured at 0, 10 and 15 s after bleaching. Visualization box size: $148 \mu\text{m} \times 148 \mu\text{m}$, resolution: 500 nm.

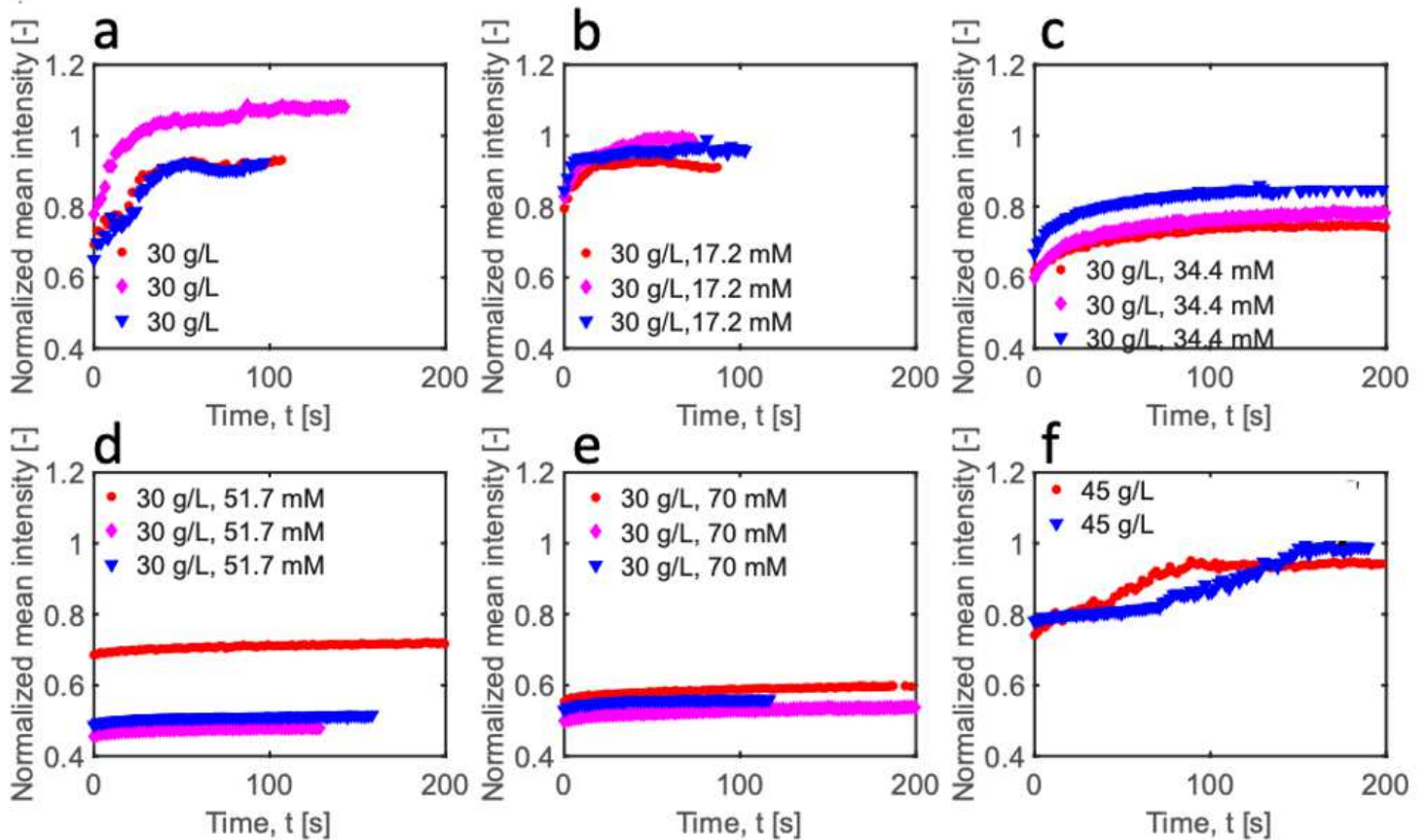


Figure 6

FRAP recovery analysis of high CNC concentration suspensions with addition of NaCl of different concentrations. (a-f) FRAP recovery curves of samples with the CNC concentrations of 45 g/L and 30 g/L at various concentrations of NaCl (0, 17.2, 34.4, 51.7, 70 mM)

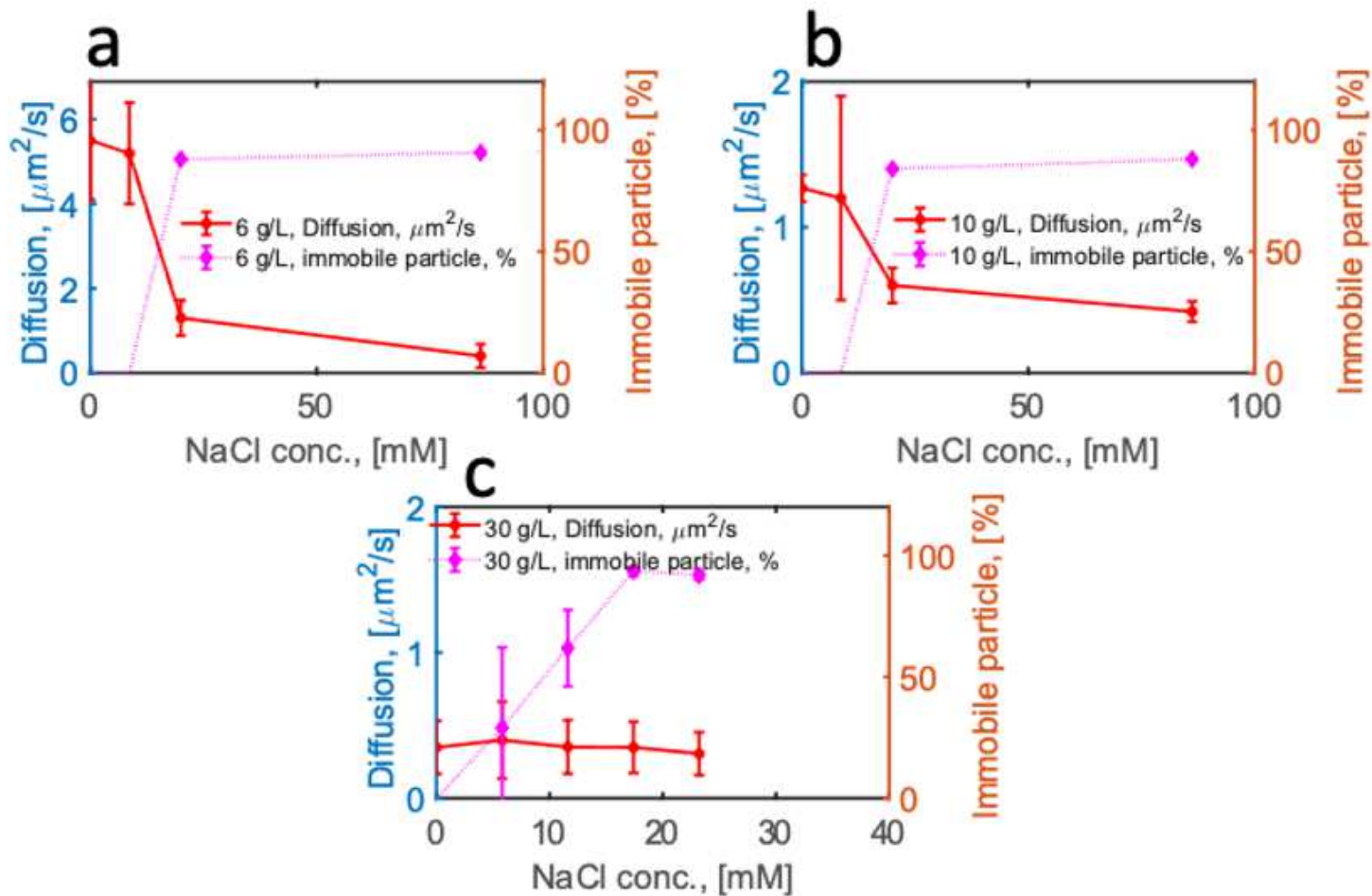


Figure 7

Variation in the diffusion coefficient and immobile particle percentage as a function of NaCl loadings (0, 8.62, 20, 86.2 mM) into the suspensions of (a) 6 g/L CNC, (b) 10 g/L CNC, and (c) 30 g/L CNC concentrations.

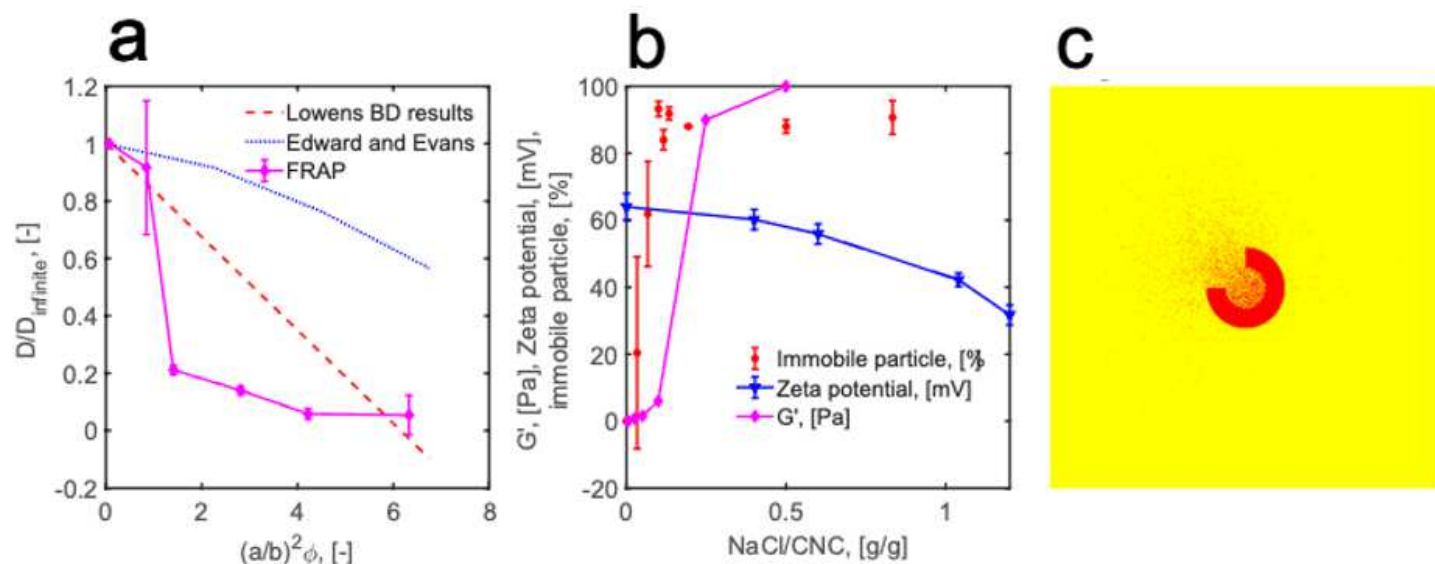


Figure 8

Comparative analysis of FRAP experiments versus other models. (a) Measured diffusion coefficients normalized by D_{infinite} , as a function of $(a/b)^2 \phi$. Note that $(a/b)^2 \phi$ is proportional to the number of rods in the volume L^3 with L the length of the rods. The results of Brownian dynamics and Edwards-Evans equation are also given as a function of concentration. (b) The universality graph that connects data of zeta potential, storage modulus, and immobile fraction obtained from the FRAP analysis. (c) The simulation presenting a path towards realization of immobile particles blockage effect on the diffusion.

Supplementary Files

This is a list of supplementary files associated with this preprint. Click to download.

- [GraphicalAbstract.png](#)
- [FRAPSI.docx](#)